Bulletin of the Seismological Society of America, Vol. 94, No. 4, pp. 1173–1194, August 2004

Ⓔ

The 14 November 2001 Kokoxili (Kunlunshan), Tibet, Earthquake: Rupture Transfer through a Large Extensional Step-Over

by Michael Antolik, Rachel E. Abercrombie, and Göran Ekström

Abstract The 14 November 2001 Kokoxili, Tibet, earthquake (M_w 7.8) ruptured ~400 km of the western Kunlun fault in northern Tibet. We apply two inversion methods to *P* and *SH* waves recorded by the Global Seismographic Network to recover the spatial and temporal history of the rupture process. The observed surface rupture consists of two strike-slip segments, offset by an extensional step-over. Little surface rupture was observed in the graben system in this step-over, which is approximately 45 km long and over 10 km wide. Our results imply that the rupture did not jump this large gap, but that the rupture was continuous through the graben. The earthquake began with a small strike-slip subevent, presumably along the westernmost of the two segments. This was followed 5 sec later by a subevent of about the same magnitude but having an oblique mechanism with a large normal-faulting component. The likely location for this subevent is within the graben. This oblique-slip event probably enabled transfer of the rupture onto the main Kunlun fault. The main moment release began ~18 sec after rupture initiation and propagated over 350 km eastward along the Kunlun fault. Slip on this segment was very heterogeneous, averaging ~2 m for the first 200 km, followed by a sharp increase to a maximum of 7.5 m within the next 50 km, and then a rapid decline. The average rupture velocity along the main segment was high (~3.6 km $\sec^{-1}$) and probably exceeded the local shear-wave velocity. The M_w 7.8 Kokoxili earthquake had a longer surface rupture and faster average rupture velocity, radiated more energy, and probably had a lower average fracture energy than the November 2002, M_w 7.9 Denali fault (Alaska) earthquake. Evidence suggests that the velocity of the rupture front dropped significantly after passing the point of maximum slip, implying a large difference in frictional strength between the two ends of the fault.

Online material: Waveform fits to teleseismic body waves.

Introduction

Within a period of 12 months, two very large strike-slip earthquakes producing surface fault ruptures exceeding 300 km in length occurred along continental plate boundaries, but fortuitously within regions of low population density. Both of these earthquakes (2001 Kokoxili, Tibet, M_w 7.8; 2002 Denali fault, Alaska, M_w 7.9) may be considered analogues for the largest earthquakes that are expected to occur along the San Andreas fault system in California. Supershear rupture velocity has been reported as likely for both earthquakes (e.g., Bouchon and Vallée, 2003; Dreger *et al.*, 2004). The Denali earthquake was well recorded at local and regional distances (McNamera *et al.*, 2002). It nucleated on a thrust fault adjacent to the main rupture (e.g., Ji *et al.*, 2002; Dreger *et al.*, 2004) and was preceded 10 days earlier by an *M* 6.7 foreshock (Eberhart-Phillips *et al.*, 2003).

The Kokoxili earthquake was not recorded at near-fault distances and only by a handful of digital recording stations at far-regional distances. It was preceded by no observed foreshocks. The earthquake occurred in a remote region of northern Tibet on the Kunlun fault, one of the major strike-slip faults that accommodate eastward movement of Tibet relative to Eurasia in response to the northward penetration of India along the Himalayas. The 2001 earthquake rupture ranks as the longest observed surface rupture for a strike-slip event (van der Voerd *et al.*, 2002a; Xu *et al.*, 2002). The total length of the surface faulting exceeded 400 km, extending from the westernmost segment of the Kunlun fault (~90.2° E) to nearly 95° E (Xu *et al.*, 2002). An average of ~2-m horizontal offset was observed, with minor amounts (generally less than 1 m) of vertical throw along the fault trace. Xu *et al.* (2002) reported a maximum offset of 7.6 m in the vicinity of Hoh Sai Hu Lake (93.3° E, Fig. 1); this

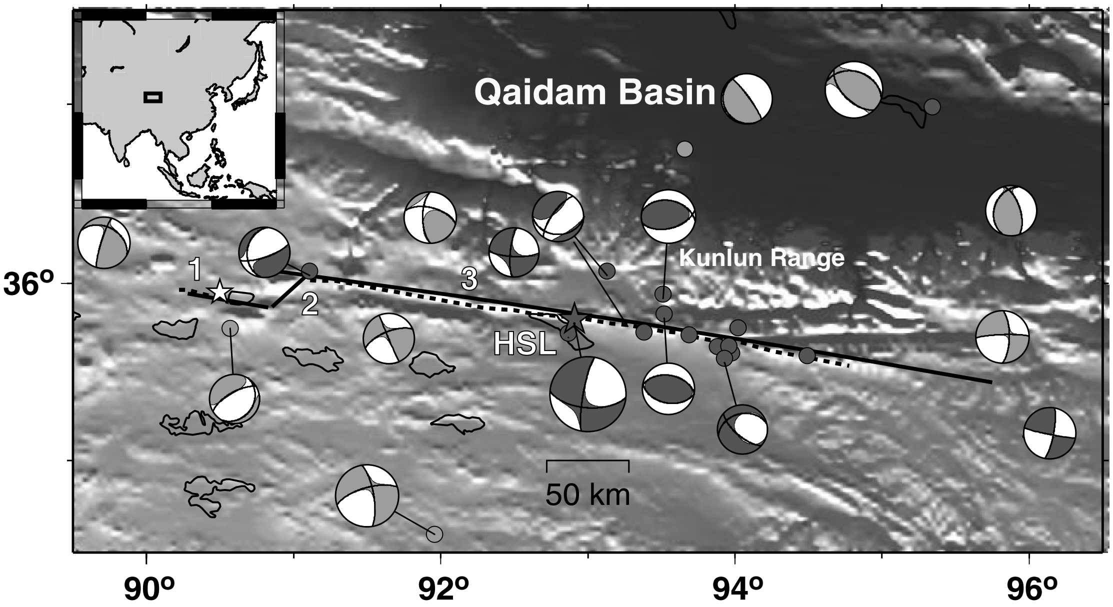

Figure 1. Generalized map of the 14 November 2001 Kokoxili, Tibet, earthquake sequence with topography. The inset shows the regional location of the earthquake. Shown is previous seismicity (light gray circles) and aftershocks occurring within 1 yr following the earthquake (dark gray circles) taken from the Advanced National Seismic System catalog along with focal mechanisms from the Harvard CMT catalog plotted in similar shade. The focal mechanism for the mainshock is shown plotted at the centroid location (gray star). The white star is the USGS hypocenter location, which is also our hypocenter for the fault inversion. The presumed fault plane of the CMT mechanism has a strike, dip, and rake of 94°, 61°, and −12°, respectively. The dashed lines show the two strike-slip surface rupture segments (after van der Woerd *et al.*, 2003). The solid black line segments represent the orientation of the fault segments that we have used for the finite-fault modeling with the surface-slip constraint, and they are numbered according to the text and figures. HSL = Hoh Sai Hu Lake.

maximum offset is similar to that observed in the Denali fault earthquake (Eberhart-Phillips *et al.*, 2003) but considerably less than the value of 16 m earlier reported by Lin *et al.* (2002).

Xu *et al.* (2002) and van der Woerd *et al.* (2003) mapped two segments of primarily horizontal slip, offset by an extensional graben (see Fig. 1). The epicenter (U.S. Geological Survey [USGS] National Earthquake Information Center [NEIC]; Chinese Seismological Bureau) is located near the western end of the surface rupture, suggesting nearly unilaterally eastward rupture propagation. The first segment of surface rupture is about 25 km long and consists of mainly left-lateral displacement. This segment is offset by 45 km to the west and 10 km to the south of the main (eastern) segment. Very little evidence of surface offset was observed in the gap (Xu *et al.*, 2002). The main segment follows the trace of the Kunlun fault for 350 km with little interruption. East of Hoh Sai Hu Lake, the main rupture segment branches from the Kunlun fault and follows a subsidiary fault (the Kunlun Pass fault; van der Woerd *et al.* [2002a]) for ~100 km. The eastward continuation of the Kunlun fault from this point has a more easterly strike (van der Woerd *et al.*, 2000) and appears not to have broken in the earthquake. In the west, the main rupture segment terminates against a large mountain massif (Buka Daban) that rises to 6800 m elevation. To the west of this massif, the Kunlun fault splays into several shorter segments that are connected by active normal faults and form an extensional graben. Some scarps with vertical throws exceeding 1 m were observed at the western end of the rupture, indicating a significant normal-faulting component. Although very little evidence of surface offsets was observed by Xu *et al.* (2002) in the large gap between the two segments, it is possible that some was missed due to the remoteness and difficulty of the terrain, or the rupture may have been continuous at depth and not broken the surface in the step-over. If no slip occurred in the graben and the mainshock rupture was able to jump such a large step-over, it would be unprecedented in observations of large strike-slip ruptures and have profound implications for models of stress transfer during rupture propagation. Harris and Day (1993, 1999) have tested numerically the ability of strike-slip ruptures to jump large step-overs, and they reached the conclusion that the widest step-over likely to be jumped is on the order of 5 km. Alternatively, it is possible that the western rupture segment results from aseismic rupture preceding or following the mainshock. Only one significant aftershock (M 5.2, 30 November 2001) was observed in the vicinity of the step-over between the two fault segments, so it is unlikely that this rupture occurred during an aftershock.

There is a significant discrepancy between published moment tensors for the Kokoxili earthquake. The Earthquake Research Institute Tokyo solution (http://wwweic.eri.u-tokyo.ac.jp/topics/200111140926) has a vertical fault plane with nearly pure strike-slip motion, while the Harvard Centroid Moment Tensor (CMT) has a fault plane that dips significantly toward the south and a small normal component (Fig. 1). Other solutions (e.g., USGS NEIC) show nearly pure dip-slip faulting, which, given the observations of the surface rupture, cannot be correct for the main part of the rupture process. These solutions were obtained using data within different frequency ranges and are probably indicative of a complex source process.

In this article we use teleseismic body waves to investigate the rupture process of the earthquake, focusing in particular on the extensional step-over. We first determine a simple model of the faulting process by describing the earthquake as a sequence of point sources. Then we investigate in detail the distribution of slip using a finite-fault inversion technique. The results from both methods are in good agreement. We compare several models that are consistent with the observed surface geometry in terms of their fit to the data and conclude that the earthquake rupture was most likely continuous through the extensional graben that lies between the strike-slip surface traces. The body waves contain evidence for a substantial change in the source mechanism over the first 15 sec of the rupture, which probably represents moment release within the extensional step-over. We also resolve a high rupture propagation velocity on the main Kunlun fault, close to and possibly exceeding the local shear-wave velocity.

Tectonic Overview

The left-lateral, strike-slip Kunlun fault extends from near 90° E to 104° E. Recent geologic evidence suggests that the long-term slip rate of the fault is 8–12 mm/yr along much of its length (94°–101° E; van der Woerd *et al.* [1998, 2000, 2002b]). This value represents between one-third and one-half of the eastward motion of the Tibetan Plateau relative to the basins to the north (Peltzer and Saucier, 1996). Thus the Kunlun fault is a major player in the internal deformation and growth of the plateau. Van der Woerd *et al.* (2000, 2002b) observed offset stream terraces reflecting cumulative offsets of up to 400 m along the central 600 km of the fault, providing evidence of repeated large to great earthquakes (M 7.5–8.0). Large earthquakes prior to 2001 in northern Tibet occurred in 1937, 1963, and 1997. The 1937 earthquake ($M \sim 7.5$) occurred on the next segment to the east of the 2001 rupture with a gap of ~200 km between them. The 1997 earthquake (M_w 7.5) occurred along the Manyi fault, which is a westward extension of the Kunlun fault but is offset ~100 km southward from the main Kunlun fault trace. This earthquake produced a 180-km-long surface rupture (Peltzer *et al.*, 1999) and a very compact distribution of moment release (Velasco *et al.*, 2000).

In addition to the left-lateral horizontal motion, approximately half of the relative convergence between the Indian subcontinent and Eurasia appears to be taken up along the northern margins of the Tibetan plateau (Meyer *et al.*, 1998; Tapponnier *et al.*, 2001). Near the Kunlun fault, this northward convergence is manifested as shortening of the Qaidam Basin, which underthrusts the Kunlun mountain range from the north (Tapponnier *et al.*, 1990; Chen *et al.*, 1999). For much of its length, the Kunlun fault runs along the southern base of the mountain front. Crustal strain partitioning in this region may explain the diversity of aftershock focal mechanisms observed for the Kokoxili earthquake (Fig. 1; Bowman *et al.*, 2003), as well as that of the background seismicity. Thrust faulting in the Kunlun range, like many of the other east–west–striking mountain ranges within Tibet, appears to accommodate crustal shortening within the plateau that may be decoupled from the mantle beneath (Tapponnier *et al.*, 2001). The various strike-slip faults that border these mountain fronts may be the surface manifestations of deep-rooted shear zones that extend completely through the lithosphere and thus divide the plateau into coherent blocks that undergo relatively little internal deformation (Wittlinger *et al.*, 1998; Holt, 2000).

Body-Wave Inversion: Point-Source Models

Data and Method

In this section we describe point-source models of the source process derived from teleseismic body waves. Our aim is to represent the earthquake with as simple a source model as can adequately fit the observed data, as well as to provide a starting model for determining the slip distribution. We start by using a single focal mechanism to describe the rupture process and find that the initial portion (first 15 sec) of the teleseismic P waves rule out such a model. Instead, we need to consider models involving additional subevents with different focal mechanisms and average rupture velocities.

Our total dataset consists of 35 P and 14 SH records form 37 stations that we obtained by removing the instrument response and deconvolving the traces to displacement. The records are provided by the IRIS/USGS Global Seismic Network (GSN) and other global networks (Geoscope, GEOFON) (Fig. 2; Ⓔ see Fig. E1–E3, online at the SSA Web site). We then apply a bandpass filter to obtain flat response between 1- and 100-sec period; these records are shown in the figures. The total source duration for the Kokoxili earthquake is comparable to the longest periods used; thus it may be desirable to employ a lower cutoff period. For each of the models discussed subsequently we repeat the inversion using a filter with a long-period cutoff at 300 sec and verify

Figure 2. Map of broadband stations used for the point-source inversions. Closed circles indicate that *P* waves only were used; open circles indicate stations from which only the *SH* phase was used. Stations from which both phases were used are indicated by the double closed symbols. The star indicates the earthquake epicenter.

that this parameter has a negligible effect on the results, including the scalar moment. To calculate the Green's functions, we use a single-layer crust of thickness 60 km with a *P*-wave velocity of 6.3 km $\sec^{-1}$ and an *S*-wave velocity of 3.5 km $\sec^{-1}$. This is similar to the Qilian Range model of Li and Mooney (1998), who found a generally thinner and more homogeneous crust for northern Tibet than southern Tibet. The receiver-side structure is Preliminary Reference Earth Model (PREM) (Dziewonski and Anderson, 1981).

Inspection of the *P* waves for the Kokoxili earthquake reveals that the moment release occurred primarily in two episodes separated by about 40 sec. The second episode represents the largest energy release and is visible at all azimuths (marked "B" in Fig. 3). The first large pulse, occurring within 20 sec of rupture initiation (marked "A" in Fig. 3), is most visible at stations located to the west and southeast from the source. It is not very visible at stations to the northeast (e.g., ADK). The relative amplitudes of the two large pulses change around the focal sphere. At stations to the west and northwest, the amplitude of the first pulse is as large or larger than the second. This provides evidence that the focal mechanisms of the two main episodes of moment release differ. Clear eastward directivity is also visible as the time difference between pulses A and B is shorter for stations located to the east of the source.

We use a method that describes the rupture process in terms of the moment tensor elements, the moment rate history, and the components of a vector **v** that describe the azimuth and speed of rupture propagation (Ekström, 1989). The directivity vector accounts for stretching or compression of the waveforms at various directions from the source. Depth is the only free hypocentral parameter. Each component of the moment rate distribution for this parameterization is

$$\dot{m}_{ij}(t, \mathbf{x}) = \hat{M}_{ij} \times F(t - t_0) \times \delta[\mathbf{x} - \mathbf{x}_0 - (t - t_0)\mathbf{v}], \quad (1)$$

where $\hat{M}$ represents the moment tensor normalized by the scalar moment and t_0 is the origin time. The source time function, $F(t)$, is parameterized as a series of overlapping triangles with a specified half-duration; we fix this half-duration to 2 sec in this study. Equation (1) can be modified to account for possible subevents having different focal mechanisms, in which case the composite moment rate tensor becomes a sum over the number of such subevents (Ekström, 1989). The number of subevents is a fixed parameter in this method, so that only the number necessary to provide an adequate fit to the data are included. This avoids the tendency for the inversion to fit crustal multiples or other phases in the body waves that are not caused by source complexity, as can sometimes occur for more complicated methods (e.g., Kikuchi and Kanamori, 1982). The maximum source duration is also a fixed parameter in each inversion but can be varied as determined by the fits to the waveforms. We also use the published Harvard CMT solution as a constraint on all of the point-source models, although it is given a very low weight in the inversion.

Single-Source Model

Figure 3 shows results from the initial inversion, which includes only a single subevent with the free parameters described earlier. We show 10 stations out of the total of 35 *P* waveforms used, representative of the full azimuthal distribution of the complete dataset (Ⓔ all of the waveforms are shown in the supplementary figures, online at the SSA Web site). The latter half of the *P* waves (including pulse B, Fig. 3) are fit with a single mechanism, which consists of left-lateral strike slip on a plane steeply dipping to the south with a very small normal component (Table 1), but the beginnings are not. This focal mechanism is very similar to the published Harvard CMT solution (Fig. 1), obtained using only very long period mantle waves. The existence of a normal-faulting component in the focal mechanism is interesting because of the discovery of normal fault scarps with modest offset (~1 m) parallel to the Kunlun fault near Hoh Sai Hu Lake (King *et al.*, 2003).

The main part of the rupture time history is well approximated by a simple triangle, with the peak in the moment release (corresponding to pulse B) occurring about 70 sec after the initiation. If we take the magnitude of the best-fitting directivity vector obtained from the inversion (3.6 km $\sec^{-1}$) as representative of the average rupture velocity, which is reasonable given the overall unilateral nature of the

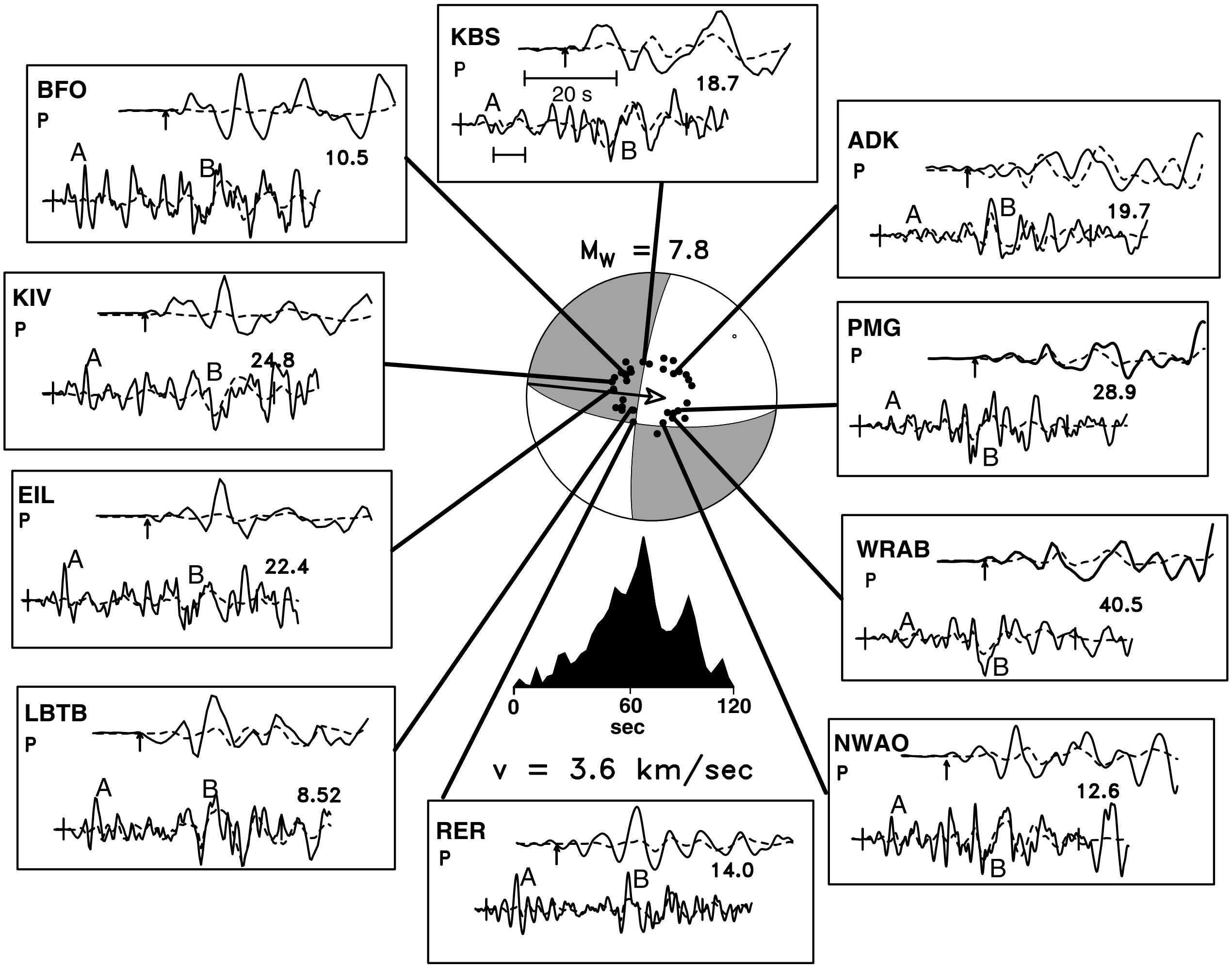

Figure 3. Point-source model for the Kokoxili earthquake allowing only one subevent, with a single focal mechanism. Ten of 35 broadband *P* waves used are shown, with two traces shown per station. Solid traces are data, and the synthetics for this model are shown as the gray dashed traces. A 20-sec timescale is shown under the traces for station KBS. Numbers at right for each station show the maximum data amplitude in micrometers. The bottom trace for each station shows the full time window used for the inversion (marked by the vertical lines), while the top trace shows the picked onset (arrow) and the following 50 sec of data. There are two dominant source pulses in the *P* waves (marked "A" and "B" as referred to in the text). While the synthetics for this model fit the last half of the used time window quite well, pulse A is not fit at most stations, as can be seen in the top set of traces. The arrow plotted on the focal mechanism represents the direction of the directivity vector determined by the inversion (3.6 km sec^{-1} at an azimuth of N95°E). The source time function for this model is sharply peaked at 70 sec after rupture initiation.

rupture propagation, then the location of the largest moment release agrees very well with the centroid location published by Harvard (Fig. 1). This directivity, as we show subsequently, is strongly required by the *P* waves, and the direction (N96°E) closely agrees with the strike of the east–west nodal plane of the source mechanism and the Kunlun fault. However, it is not at all clear in this model where pulse A occurs in the source time function, and the first 20 sec of the *P* waves are not well fit, except at stations to the northeast where the amplitude of pulse A is small. The first 20 sec of the source time function has very low amplitudes, representing only about 5% of the total moment release. Because of the very poor fit to the early portion of the *P* waves, we must consider more complicated models containing additional subevents.

Multiple-Source Models

We can use the polarities of the recorded first motions to help constrain the focal mechanism for the initial portion of the rupture process. The contemporary station coverage

Table 1
Point-Source Model Parameters

	One-Source Model	Two-Source Model	Three-Source Model
Subevent 1			
Strike/dip/rake (°)	96/71/−9:189/82/−161	270/90/0:0/90/−180	271/81/−4:1/86/−171
Depth (km)	13 ± 4	9 ± 3	9 ± 3
V_{r} (km sec^{-1})	3.6 ± 0.5	2.0 ± 1.0	2.0 ± 1.0
M_{o}(10^{20} N m)	5.26	0.22	0.13
Subevent 2			
Strike/dip/rake (°)	—	96/71/−9:189/82/−161	282/62/−41:34/54/−145
Depth (km)	—	12 ± 4	5–11
V_{r} (km sec^{-1})	—	3.4 ± 0.8	0–2
M_{o} (10^{20} N m)	—	5.15	0.09
Subevent 3			
Strike/dip/rake (°)	—	—	96/74/−10:189/80/−164
Depth (km)	—	—	12 ± 4
V_{r} (km sec^{-1})	—	—	3.1–4.3
M_{o} (10^{20} N m)	—	—	5.05
VR (%)	29.5	31.1	36.5

VR is variance reduction to the data; V_{r} is rupture velocity. Uncertainties reflect a 10% decrease in VR.

provided by the GSN is sufficient that first-motion mechanisms for strike-slip earthquakes can often be tightly constrained (e.g., Antolik *et al.*, 2000; Abercrombie *et al.*, 2003). From the waveforms that are depicted in Figure 3, it is obvious that the first-motion mechanism must be strike slip. For example, note the change from positive to negative polarities from KIV to LBTB. However, the nodal planes cannot have the same orientation as the single point-source focal mechanism since the southern Pacific stations (PMG, WRAB) would have the wrong polarity in that case. In Figure 4 we plot first-motion polarities at all available teleseismic stations, as well as four regional-distance stations (10°–20°). The teleseismic observations constrain the strike of the east–west nodal plane to lie within 10° of 270° (or 90°), and it must be either vertical or have a steep dip to the north (>80°). The regional stations are all consistent with this mechanism. This is in contrast to the focal mechanism in our single-source model, in which the east–west–striking plane dips to the south. In addition, the slip angle must lie within 5° of pure strike slip (0°) to satisfy the polarities of stations in northeast Asia and Alaska. The focal mechanisms depicted in Figure 4 are all consistent with the short segment of left-lateral surface rupture observed at the western edge of the rupture by Xu *et al.* (2002) and would also agree with the Earthquake Research Institute (ERI) Tokyo moment tensor solution.

Figure 5 shows the fits to the same waveforms shown in Figure 3, but for a source model consisting of two subevents. The first subevent has a fixed duration of 25 sec, and the focal mechanism was fixed to the first-motion mechanism in Figure 4a. That leaves only the source time function, depth, and directivity vector to be determined by the inversion (if we allow the focal mechanism to vary, then a focal mechanism that violates the first-motion polarity constraints is obtained). The source time function for the first subevent determined from this analysis consists mainly of two pulses

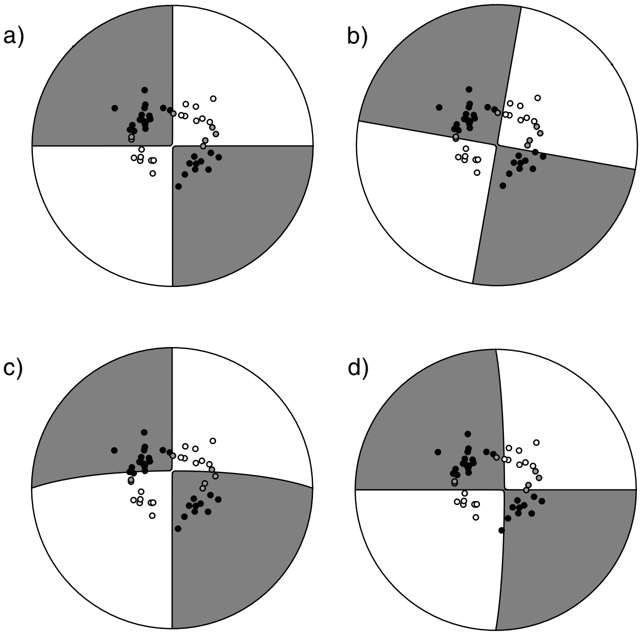

Figure 4. Range of possible focal mechanisms that fit the first-motion polarity observations at teleseismic and regional distances. Filled circles indicate compressions, open circles indicate dilatations, and gray circles denote unclear polarities. The observations constrain the strike of the East–West nodal plane to be in the range 270°–280°, the dip to be >80°, and the rake angle to lie within 0 ± 5° (pure strike-slip motion). (a) Strike 270°, dip 90°, rake 0°; (b) strike 280°, dip 90°, rake: 0°; (c) strike 270°, dip 80°, rake 0°; (d) strike 280°, dip 90°, rake − 5°.

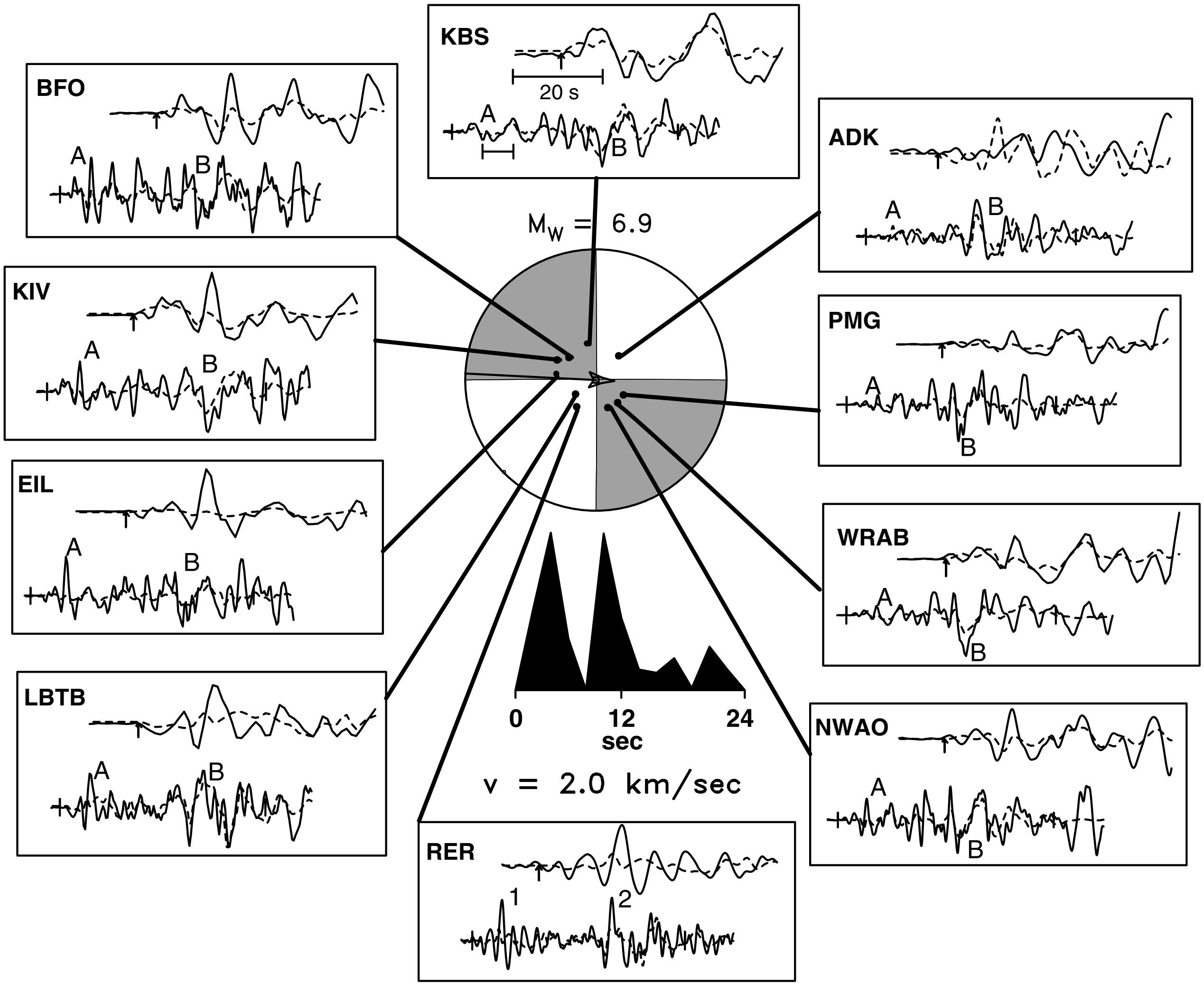

Figure 5. Source model consisting of two subevents. The first subevent has been fixed to the focal mechanism of Figure 4a. The focal mechanism and moment rate function shown are for the first subevent only. The waveforms shown are for the same stations as in Figure 3. Other symbols are the same as in Figure 3. The fit to the first 50 sec of the *P* waves is not improved significantly over the single-subevent model (top traces).

with a total duration of around 15 sec. The second subevent covers the remainder of the rupture process and is fixed to the same moment tensor as derived in the single point-source model. The source time function is similar to the single-source model. Figure 5 shows that the fit to pulse A in the *P* waves is not significantly improved by this model. In fact, as we demonstrate later, the fit cannot be improved upon significantly using any of the possible focal mechanisms that fit the first-motion polarities for the first subevent.

We therefore add a third subevent to the rupture model and allow all four parameters (moment tensor, source time function, depth, and directivity vector) to be freely determined for each subevent. We also offset the first subevent representing the initial break by 10 km south and 40 km to the west of the third and largest subevent to represent the rupture geometry described by Xu *et al.* (2002). The fit to the data for this three-source model is shown in Figure 6. We allow the first two subevents to overlap in time in this model, but separation of the moment release into two pulses over the first 15 sec (as in Fig. 5) is still evident. There is little moment release in the second subevent before 6 sec. Also, the third and largest subevent was constrained to begin 15 sec after the rupture initiation, in accordance with the time history derived in the single-source model. Subevent 2 consists primarily of a single pulse with about 8-sec duration. Extending the duration of the second subevent to 30 sec (partially overlapping with subevent 3) improves the fit to the *P* waves. This subevent has a highly oblique focal mechanism (rake = −40°) and nodal planes having a shallower dip and thus differs significantly from the focal mechanisms for the other two subevents. This focal mechanism matches pulse A quite well. There is no resolvable directivity

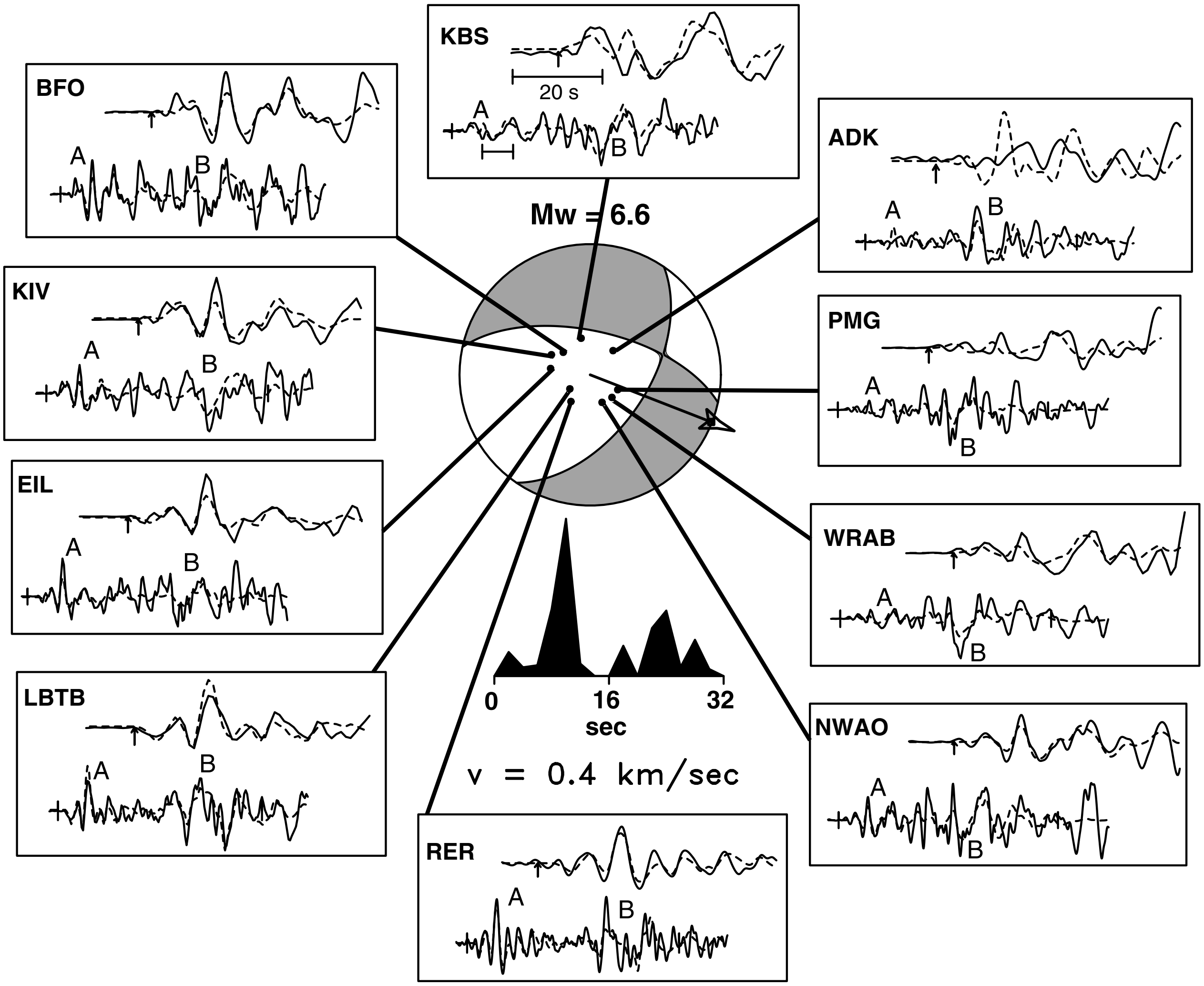

Figure 6. Source model consisting of three subevents. The focal mechanism and moment rate function shown are for the second subevent, which consists of oblique motion with a large normal-faulting component. Other symbols are the same as Figure 3. This model fits the first 50 sec of the *P* waves well. Other details of the model are explained in the text.

for this second subevent. The focal mechanism of the third subevent remains virtually unchanged from the single-source model. Including a second subevent within the first 15 sec of the rupture process allows a focal mechanism to be obtained for the first subevent that agrees with the observed first-motion polarities without imposing this constraint on the inversion.

The parameters of the three-source model are listed in Table 1 and shown in Figure 7. Combined, the first two subevents represent ~5% of the total seismic moment (M_w 7.8). The total variance reduction is 36%. This model improves the variance reduction over the two-subevent model by ~5%, all of which results from the fit to the first 15 sec of the *P* waves (considering only the first 50 sec, the improvement in misfit is much larger; see Fig. 8). Because of the large normal-faulting component in subevent 2, its presence in the model makes a significant difference in the fit to the data, even though its moment is smaller than subevent 1. The first strike-slip subevent does not contribute much to the *P* waveforms because of its small size (compared to the subsequent main moment release) and because of the proximity of many of the stations to a nodal plane. Even with this level of complexity, there are portions of the *P* waves that are still not particularly well matched. However, the two dominant pulses are now well fit, and thus we do not consider more complex models. In view of the observations of King *et al.* (2003), it may be possible to make further improvements in the fit to the later portion of the *P* waves by allowing additional subevents (perhaps involving normal faulting) in the source process, but we do not feel it is justified given the large increase in the number of free parameters that would be required.

Next, we determine the degree of focal mechanism change required during the first 15 sec of rupture by invert-

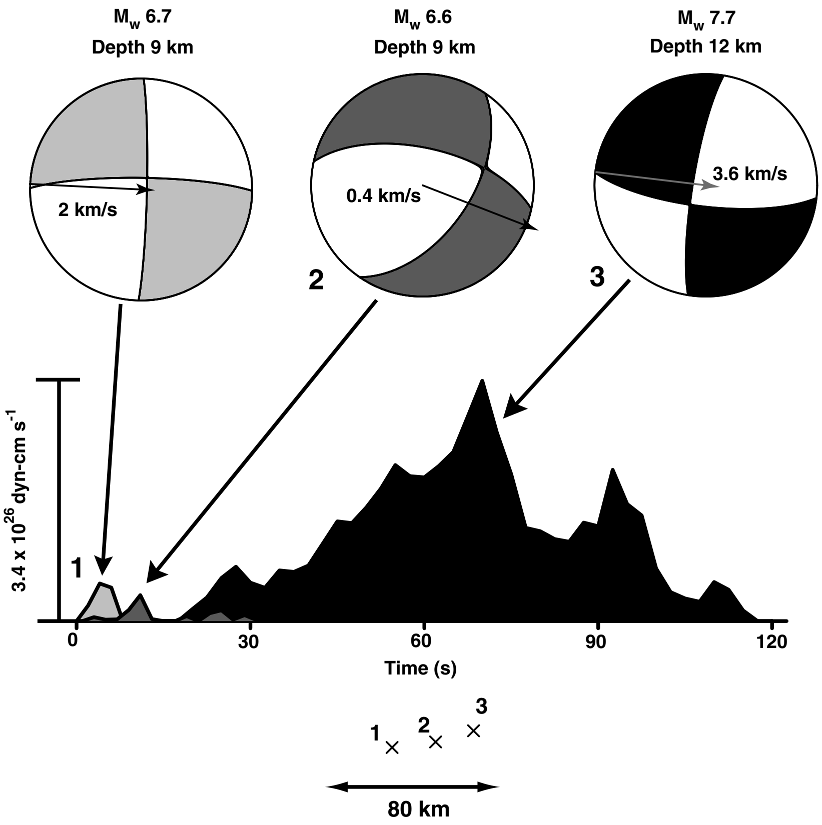

Figure 7. Representation of the preferred three-subevent point-source model of the Kokoxili earthquake. In this model all three subevents have a freely determined focal mechanism. The first subevent has a duration (fixed) of 6 sec. The second subevent is constrained to begin at the rupture initiation and terminate 30 sec later; however most of the moment release occurs after 5 sec and before 15 sec (after rupture initiation). The third subevent is constrained to begin rupturing 15 sec after initiation. Shading in the moment rate function matches that of the focal mechanisms (first subevent, light gray; second subevent, dark gray; third subevent, black). Magnitudes, depths, and directivity vectors of each subevent are also shown. The relative locations between the subevents are shown at the bottom. These locations were assigned based on mapping of the surface rupture (Xu *et al.*, 2002).

ing only the initial portion of the *P* waves. For this analysis, we use the time window beginning 5 sec before and ending 50 sec after the picked onset. In this time window the dominant arrival is pulse A, and so the results will be controlled by the degree of fit to this arrival (Fig. 3). Figure 8 shows the resulting misfit to the data as the dip and rake angles are varied for a fault plane that we assume strikes east–west (in accordance with the first-motion polarity constraints). In all cases, the other parameters in the inversion are allowed to vary. The minimum normalized misfit (0.56) occurs for planes dipping between 60° and 65° (toward the north) and with a rake angle between $-35°$ and $-40°$, similar to the parameters determined for subevent 2. The dip must be shallower than 75° and the rake angle steeper than $-20°$ (on this plane) in order to produce a residual misfit no greater than 10% larger than provided by the best-fitting solution. Since the rake of the first-motion mechanism is constrained to depart from pure strike-slip by no more than 5° (Fig. 4), we conclude that a change in focal mechanism between the rupture initiation and generation of pulse A is required by the *P* waves. The range of focal mechanisms that are consistent with the first-motion polarities requires at least a 30% increase in the misfit.

Comparison of the Preferred Model with the Surface Rupture

Our preferred solution is in good qualitative agreement with the mapped surface rupture on the two segments. We have offset the locations of the first two subevents in Figure 7 to match the rupture geometry from field observations (Xu *et al.*, 2002; van der Woerd *et al.*, 2003), but the exact relative locations of these subevents are not constrained by the teleseismic observations. Although the initial rupture of the earthquake is clearly strike slip, we cannot determine whether the initial rupture was unilateral or bilateral. We also cannot determine the precise onset time of the oblique rupture mechanism, although it must be within the first 5 sec in order to fit pulse A in the *P* waves.

The epicentral location (Fig. 1) lies close to the short western segment of surface rupture and would be consistent with initiation on this segment (van der Woerd *et al.*, 2002a). The moment magnitude of the first subevent (M_w 6.7) is also consistent with the length of the western surface-rupture segment (26 km). Significant vertical offsets were not observed on this segment (Xu *et al.*, 2002), so the location of the second subevent is most likely to the east, within the step-over between the strike-slip segments. This interpretation is consistent with the horsetail extensional graben that exists between these two segments. It is likely that the oblique second subevent provided the means to transfer slip from the western segment through the gap and around the Buka Daban massif to the main Kunlun fault. Rupture then occurred to the east along the Kunlun fault in a fairly smooth process, as evidenced by the sharply peaked source time function.

Average Rupture Velocity

All of the preceding rupture models include a rupture velocity of ~3.6 km $\sec^{-1}$ on the main rupture segment.

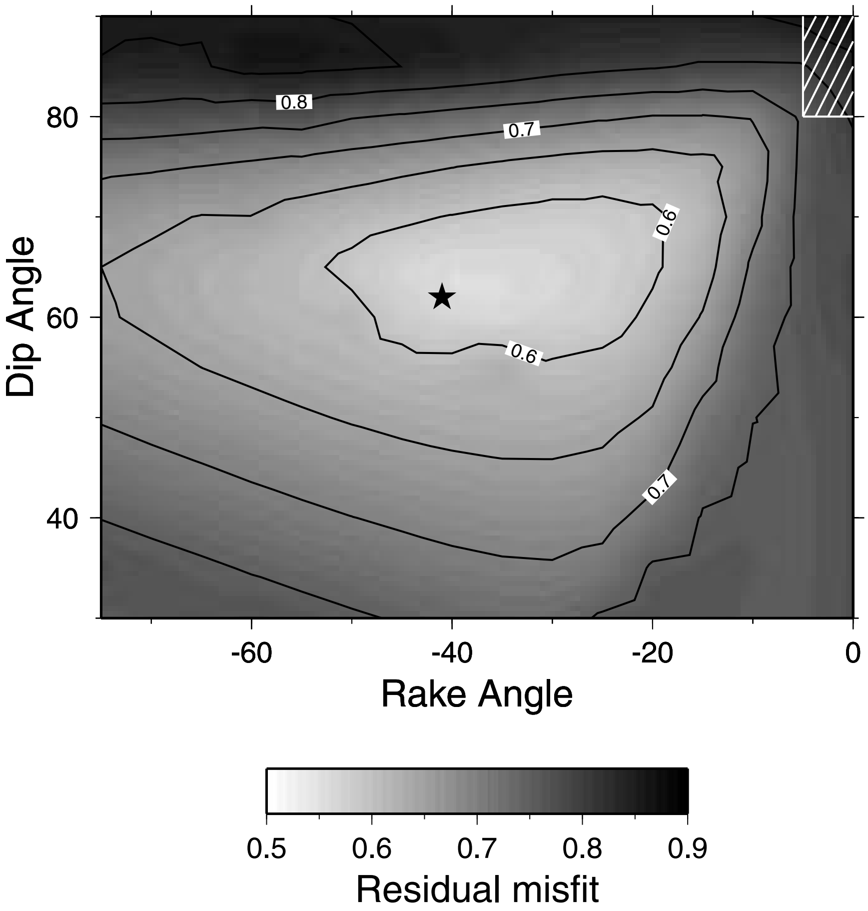

Figure 8. Examination of the model space for inversion of the first 50 sec of the *P* waves. Shown are contours of the normalized residual misfit for different values of dip and rake angle on the east–west–striking plane of the focal mechanism. The strike of the plane is fixed at 270°. The star indicates the values of dip and rake corresponding to the second subevent for the preferred three-subevent model (shown in Figs. 6 and 7). In order to produce a misfit no larger than 10% higher than the best-fitting solution, the dip can be no larger than ~75°, and the rake must differ from pure strike slip by at least 20°. Note that the elongated pattern of the misfit surface shows that a focal mechanism close to pure normal faulting is more permitted by the data than a pure strike-slip focal mechanism. The white hatched region in the upper right shows the range of mechanisms that fit the first-motion polarities. Therefore the focal mechanism change described in the three-subevent model is required by the *P* waves.

Rupture propagation at this speed would likely exceed the local shear-wave velocity. In analysis of seismograms from far-regional stations, Bouchon and Vallée (2003) concluded that supershear rupture for a large portion of the Kokoxili earthquake was required. Their average velocity for the entire rupture was 3.7–3.9 km sec^{-1}, with locally higher values (as high as 5 km sec^{-1}). The difference between our average rupture velocity and that of Bouchon and Vallée (2003) is certainly within the uncertainties of both methods.

The rupture occurred primarily through alluvial fans emanating from the steep Kunlun range front (Xu *et al.*, 2002), which would make supershear rupture speed even more likely given the probable low shear velocity in these sediments. These sediments can be up to several kilometers thick in regions of Tibet (e.g., Meyer *et al.*, 1998). The distance of the maximum slip from the rupture initiation (~250 km), combined with the rather late onset for the main moment release after rupture initiation (~18 sec), also suggest a very high velocity for part of the rupture.

To examine the constraints on the rupture speed, we repeat the point-source inversion, fixing the directivity vector in the largest subevent to a range of values (Fig. 9). The variance curve has a sharp minimum, and so we conclude that the teleseismic observations are consistent with supershear rupture propagation. However, the teleseismic data do not support the very high rupture velocity (5 km sec^{-1}) obtained by Bouchon and Vallée (2003) for three segments of their four-segment model. Those three segments roughly

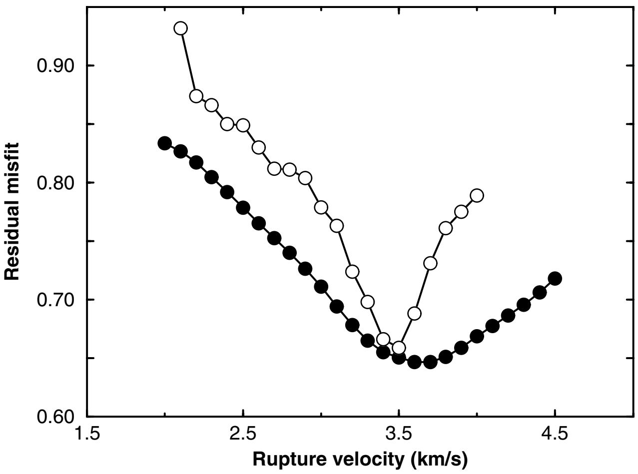

Figure 9. Normalized residual misfit for various assumed rupture velocities for the third and largest subevent. The curve with closed circles denotes the point-source results, while the curve with open circles is from the finite-source modeling. The data set used is different for the two methods. The point-source analysis used 49 *P* and *SH* waveforms, while the finite-fault inversion employed *P*-wave records from 21 stations. Both methods suggest a high rupture velocity for the third subevent.

correspond to our third subevent. Such a rupture speed for the third subevent results in more than a 20% increase in the misfit.

Body-Wave Inversion: Slip Distribution

In this section, we develop a distributed-slip model for the Kokoxili earthquake based on the point-source results and the observed surface-rupture geometry. We invert a subset of the teleseismic *P* waves using a finite-fault method similar to other studies (e.g., Wald and Heaton, 1994; Kaverina *et al.*, 2002; Antolik and Dreger, 2003). The rupture is divided into three fault segments, whose orientations are determined by the focal mechanism solutions from the previous section. We use the USGS hypocenter location (35.9° N, 90.5° E) as the starting point for the rupture. The segments are numbered according to the order in which rupture is initiated. Rupture begins on fault segment 1, with fault segment 2 following 5 sec later, in order to remain consistent with the three-subevent model presented in Figure 7. We allowed the main segment 3 to begin rupturing at the origin time, to see whether the *P* waves require any slip on this segment before the onset of subevent 3 (they do not). On all three segments, we constrained the focal mechanism to that determined from the point-source model. The segments are divided into nodes with a dimension of 5 km along both the strike and down-dip directions. Because of the lack of near-source data to constrain details of the source process, we use a simple model where the rupture is constrained to propagate at a constant velocity from the hypocenter. The slip history of each node is an isosceles triangle with a constant duration, and each node is allowed to slip only once as the (circular) rupture front passes. The synthetic seismogram for each node is obtained from a sum of five point sources distributed along strike and delayed according to the rupture front propagation.

We use a modified reflectivity algorithm to compute the Green's functions for the inversion (e.g., Saikia, 1994), employing the simple source-side crustal structure from the previous analysis, while the Iasp91 model (Kennett and Engdahl, 1991) is used for the mantle. The response of the entire mantle is included in the calculation so that core reflections (*PcP*) and other possible interfering phases are present in the Green's functions. Attenuation is included through the radial model QL6 (Durek and Ekström, 1996). The inversion method is a linearized scheme that places several constraints on the solution. The constraints employed here include slip positivity, spatial-gradient smoothing, and a requirement that the scalar moment be close to the value obtained in the point-source model. The total system of equations therefore differs slightly from that in Antolik and Dreger (2003) and Wald and Heaton (1994):

$$\begin{pmatrix} \mathbf{W}\cdot\mathbf{G} \\ \lambda\mathbf{D} \\ \eta\mathbf{i}^{\mathrm{T}} \end{pmatrix} (\mathbf{m}) = \begin{pmatrix} \mathbf{Wd} \\ 0 \\ M_0^{3\mathrm{S}} \end{pmatrix}, \qquad (2)$$

where the matrix $\mathbf{G}$ consists of the Green's functions, $\mathbf{W}$ weights and normalizes the data, and $\mathbf{D}$ is a gradient smoothing matrix for both coordinate directions. The constants λ and η control the weighting of the constraints relative to the data fit. The slip-positivity constraint requires $\mathbf{m} \geq 0$, indicating slip along the rake direction. The components of the vector $\mathbf{i}$ all equal unity, which encourages a solution having a total scalar moment close to the value obtained in the three-subevent point-source model ($M_0^{3\mathrm{S}}$). The data vector $\mathbf{d}$ consists of 150 sec of the broadband *P* waves from 21 stations. Fourteen of the stations used in the point-source analysis were omitted in order to achieve a more balanced azimuthal distribution.

Inversions of this type typically include a constraint that minimizes the total scalar moment and reduces spurious slip in the solution resulting from unmodeled wave-propagation effects (e.g., Wald and Heaton, 1994). However, inversion of body waves (even from broadband recordings) can be relatively insensitive to longer-period aspects of the source process and thus seriously underestimate the scalar moment (Ekström, 1989; Lay and Wallace, 1995). This is particularly true for earthquakes having a very long duration, such as the Kokoxili event. Without the constraint applied to the scalar moment, the distributed-slip inversion repeatedly resulted in scalar moment values less than that obtained from the point-source inversion. This constraint therefore ensures consistency between the two results.

The preferred solution, shown in Figure 10, is obtained by searching the model space for the best average rupture velocity and slip duration by means of repeated inversions. Even with the constraint on the total moment, the slip is heavily concentrated into a few small regions of the fault. The slip primarily occurs on a 70-km-wide patch that is centered roughly 225 km to the east of the hypocenter. This large asperity corresponds to pulse B on the waveforms shown in Figure 3. Its position agrees well with the timing of the large peak in the source time function 70 sec after rupture initiation (Fig. 7). The maximum value of slip is about 10 m, larger than the maximum surface offset of 7.6 m reported by Xu *et al.* (2002). We varied the rupture velocity imposed on the inversion by increments of 0.1 km $\sec^{-1}$, and the variance curve has an even sharper minimum than for the point-source analysis (Fig. 9). The rupture velocity of the best model (3.6 km $\sec^{-1}$) is consistent with the point-source analysis, however. The first two fault segments contain relatively minor amounts of slip (maximum slip of 3.0 m on fault 1 and 1.8 m on fault 2). Other asperities (regions of concentrated moment release) in this model exist at about $x = 50$ km (near the western edge of the observed surface slip on the main fault segment) and at about $x = 400$ km. The best averaged rise time (slip duration) of the model is 3 sec, but this value is not well constrained.

Surface-Slip Constraint

The slip-inversion results are in excellent agreement with the point-source model, but Figure 11 shows that the estimated surface slip does not match the observations (Xu *et al.*, 2002) well. The largest asperity in the fault model occurs at the location of maximum observed slip, but substantial slip (an average of about 2 m) between the asperities was discovered in the field. We therefore use the observed surface rupture as an additional constraint on the inversion result. This constraint takes the form of

$$\mathbf{m}_0 = \mathbf{W}^S \cdot \mathbf{x}^S, \tag{3}$$

where $\mathbf{m}_0$ represents model values for the top row of fault nodes, $\mathbf{x}^S$ is the vector of surface offset measurements taken by Xu *et al.* (2002), and $\mathbf{W}^S$ is a weighting matrix. Each row of $\mathbf{W}^S$ contains a nonzero entry for each surface-offset measurement taken within 5 km of the corresponding fault

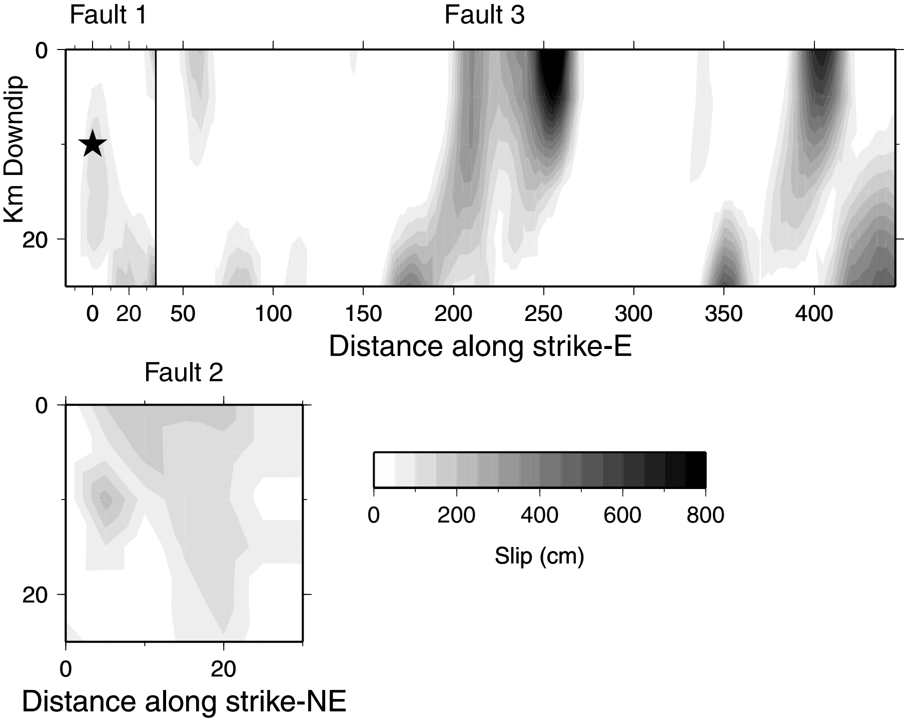

Figure 10. Slip distribution of the Kokoxili earthquake obtained using least-squares inversion with no constraint on slip at the surface. The fault segments are numbered as in Figure 1 and according to the three subevents depicted in Figure 7. The fault orientations for this inversion used the focal mechanisms obtained for the three subevents in the point-source model. Fault segments 1 and 3 overlap by ~20 km, but we have used a common coordinate system to plot both segments (kilometers east-southeast from the hypocenter located on segment 1 [star]). The horizontal scale is also given in terms of longitude for comparison with Figure 1. Fault segment 2 intersects segment 3 at $x = 48$ km. The rake angle on each segment is fixed according to the focal mechanisms of the subevents in Figure 7. See text for other details.

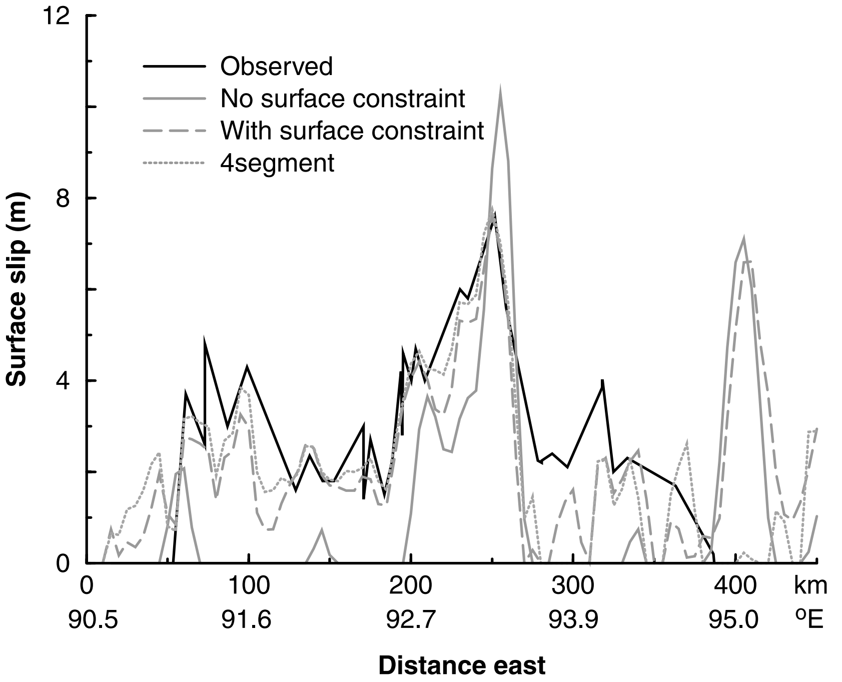

Figure 11. Surface-rupture distribution of the Kokoxili earthquake as mapped by Xu *et al.* (2002) and plotted according to the coordinate system used for fault segments 1 and 3 in Figure 10 (solid black curve). The gray curves show the distribution of surface slip from the models presented in Figure 10 (solid gray), Figure 12 (dashed gray), and Figure 15 (dotted gray).

node's location that depends on the distance from the measurement. In zones where multiple measurements are available nearby, this ensures that all observations are taken into account and helps to minimize the effects of uncertainties in the offset measurements. The vector $\mathbf{m}_0$ includes only those fault nodes that lie within 5 km of at least one measurement, so that gaps in the measurements remain unconstrained. This constraint is applied only to fault segment 3 since Xu *et al.* (2002) did not report locations of any measurements taken on the short western fault segment. In addition, we used the strikes of the observed surface ruptures (280° and 99°, respectively) for fault segments 1 and 3, rather than those obtained from the point-source model. The locations of the fault segments for this model are shown in Figure 1.

Figure 12 shows the result of an inversion including the surface-slip constraint. Models that agree closely with the observed surface-slip distribution (Fig. 11) do not cause significant degradation of the fit to the seismograms. The general distribution of the asperities in this model is very similar to that shown in Figure 10. The total slip in the largest patch of moment release ($x = 200$–250 km) is smaller, and the maximum slip of 7.7 m is compatible with the largest mapped offset. The moment removed from the largest asperity has been distributed into the regions that previously were devoid of slip. To achieve a relative proportion of moment release on fault segments 1 and 2 that is compatible with the three-subevent model, it is necessary to impose this partitioning constraint on the inversion. This accounts for the slightly higher moment on fault segment 1 (and smaller moment on segment 2) for this model. The large asperity present at the eastern end of segment 3 ($x = 400$ km) remains, even though it is located past the eastern edge of the observed surface offset. The contribution of this asperity to the data fits occurs after 100 sec and is visible on records at east and northeast azimuths in Figure 13. Although the existence of this asperity is equivocal, we have included it in the slip models because its removal causes a visible decrease in the fit to this portion of the data. We discuss this issue further later.

Discussion

Our results from the previous two sections show that at least three subevents are required to fit the teleseismic data. The second subevent has a distinctly different focal mechanism from the other two, with a significant normal-faulting component. The average propagation velocity on the main rupture segment is about 3.6 km sec^{-1} and probably exceeded the shear-wave velocity for a large portion of the source duration. In this section we discuss the implications of these results.

Model Uncertainties

Comparison of Figures 10 and 12 indicates that the distributed-slip inversion can constrain only the location and strength of the largest asperities along the fault, not the details of the rupture wherever there are low levels of slip. Forward modeling results suggest that slip uncertainties are about 1 m on segment 2 and about 2 m within the largest asperity. Outside of the large asperities ($x = 200$–250 km and $x = 400$ km), the uncertainty in the level of slip is on the order of 3–4 m. The data are most sensitive to the slip on fault segment 2 and in the largest asperity since these constitute the largest contribution to the body waves. The slip on segment 1 has the largest uncertainty. Even doubling

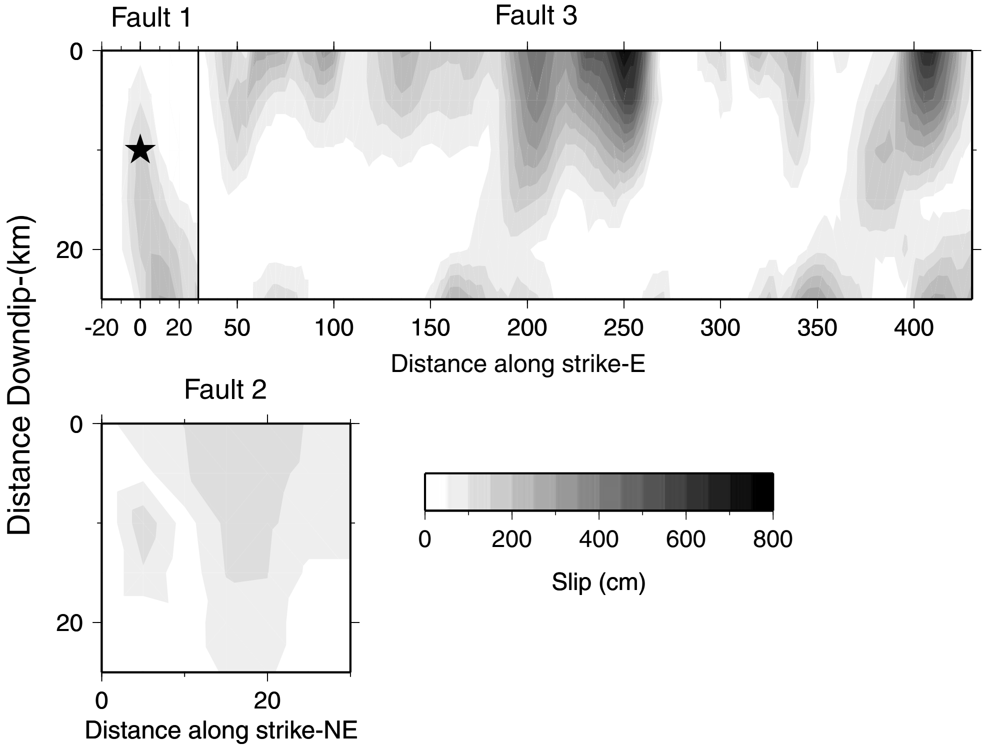

Figure 12. Slip distribution obtained from finite-fault modeling including constraint on the surface slip. Form is the same as Figure 10. The overall slip pattern is similar to Figure 10 but with significant slip occurring between the largest asperities.

the scalar moment on segment 1 does not significantly decrease the data fits, primarily because many of the seismograms lie near a nodal plane for this focal mechanism and thus are relatively insensitive to slip on this segment. These uncertainty estimates do not include additional errors that may result from fixing the focal mechanism of each fault segment. Figure 8, for example, shows that the range of acceptable rake angles for fault segment 2 is ~30°. We also do not know which nodal plane of the focal mechanism for this subevent is the correct fault plane. This unfavorable situation can probably not be rectified without the use of near-fault recordings or observations of the static deformation field (Global Positioning System, Interferometric Synthetic Aperture Radar [InSAR]). In their inversion of InSAR data, Lasserre *et al.* (2003) found larger slip values in the region of fault segment 1 and in the 200-km-long region between the hypocenter and the largest asperity (maximum ~5 m). Their inversion is not well constrained here, however, because the data coverage around the western end of the surface rupture is sparse. Inversions using geodetic data can also be susceptible to the mapping of postseismic slip into the mainshock.

The large uncertainty in the amount of slip between the asperities is reflected in the fact that the difference between the variance reduction provided by the models of Figures 10 and 12 is only 2.5%, and as is seen in Figure 13, there is no significant difference in the visible fit to the data. Figure 12 shows our preferred slip model since it is consistent with both the surface-offset data and the three-subevent model. Slip distributions obtained from different data types often differ significantly for the same earthquake (Wald *et al.*, 1996; Delouis *et al.*, 2002; Kaverina *et al.*, 2002), with seismic data frequently permitting less slip between asperities than geodetic data (e.g., Kaverina *et al.*, 2002; Eberhart-Phillips *et al.*, 2003), even when near-fault recordings are available. Without the information provided by the mapped surface slip, we might have interpreted the main fault slip (segment 3) as a segmented rupture on multiple strike-slip faults. Henry *et al.* (2000) made such an interpretation based on teleseismic body and long-period surface waves for the 1998 Antarctic Plate earthquake. However, Hjörleifsdóttir *et al.* (2003) used numerical three-dimensional modeling of long-period surface waves to demonstrate that significant slip occurred in between the two large asperities in that case.

Rupture of the Extensional Step-Over

The teleseismic *P* waves for the Kokoxili earthquake require a substantial change in the focal mechanism during the first 15 sec of the rupture, from nearly pure strike slip (subevent 1) to oblique slip with nearly equal components of normal and strike-slip faulting (subevent 2), but they do not constrain the location of the oblique slip. The coseismic

a) No surface slip constraint

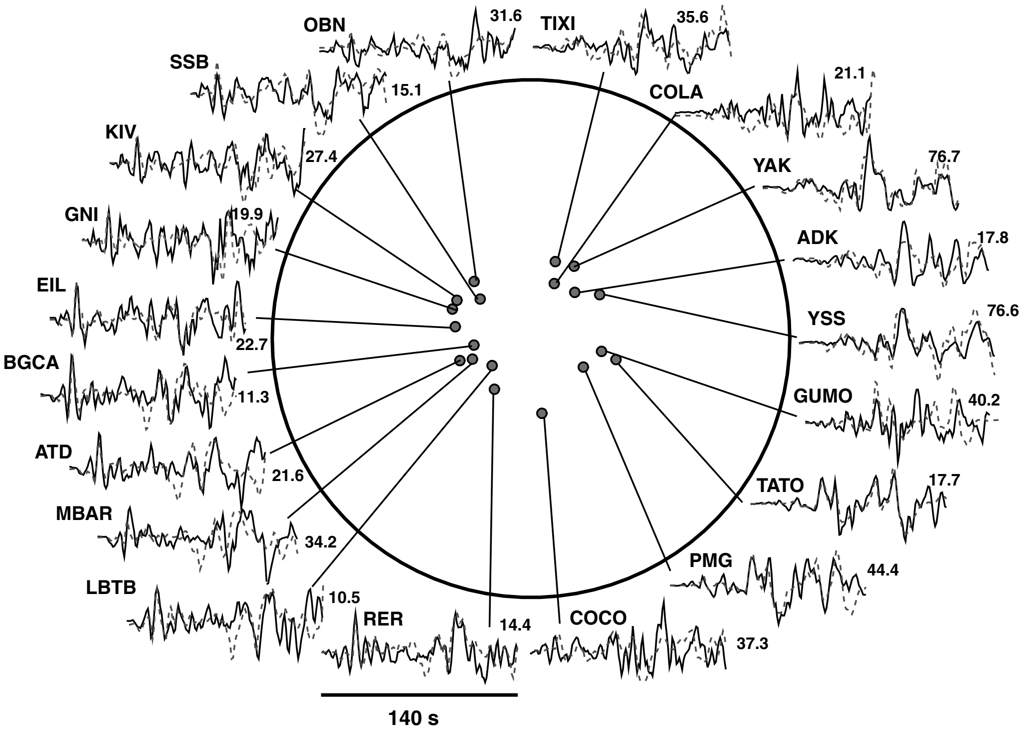

b) With surface slip constraint

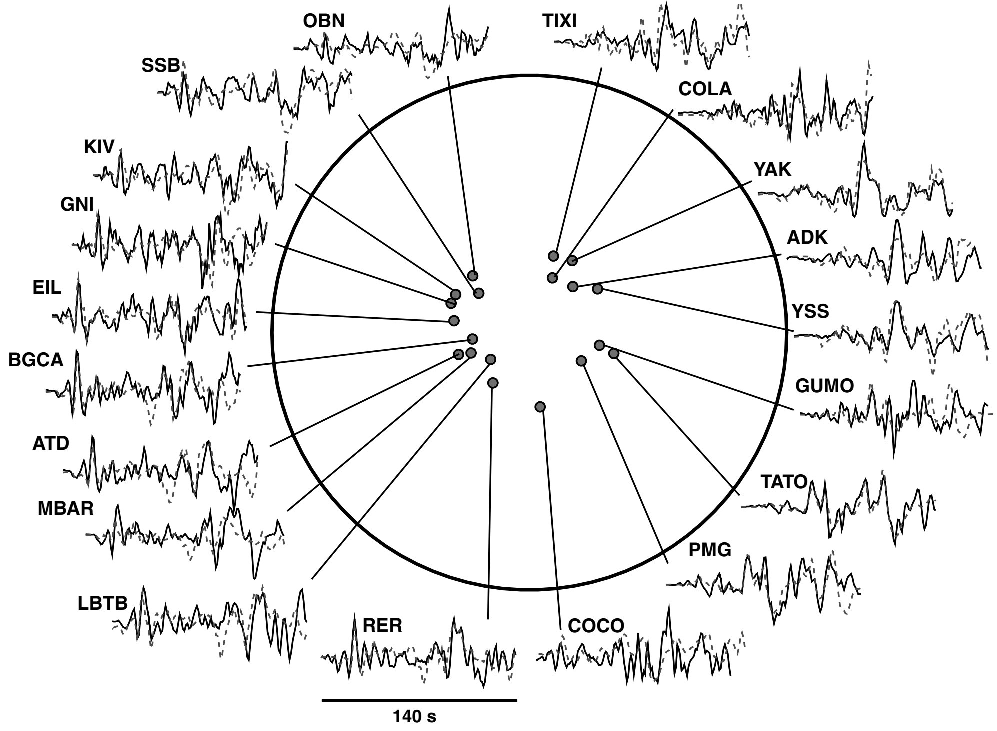

Figure 13. *P* waves (solid) used in the finite-fault modeling and synthetic seismograms (dashed). Entire time window used for each station is shown. The numbers at the right of the traces are maximum amplitudes in micrometers. (a) Fault model without surface-slip constraint. (b) Fault model including surface-slip constraint.

vertical offset on the western strike-slip rupture segment is less than 0.5 m (Xu *et al.*, 2002), compared to greater than 1 m of left-lateral slip, which makes it unlikely that the oblique-mechanism subevent represents slip on this segment. The gap between the two strike-slip rupture segments mapped by Xu *et al.* (2002) is ~45 km long and at least 10 km wide, easily big enough to contain the subevent of M_w ~6.6 that we obtain in the point-source analysis. Within this gap lies an extensional graben that contains many mapped faults, which generally strike within about 20° of East–West and some of which show significant vertical offsets. Coseismic subsidence of the extensional graben on the order of 2 m apparently occurred (van der Woerd *et al.*, 2003). Normal-faulting earthquakes with mechanisms similar to subevent 2 have occurred in this region in the past, and the only large aftershock of the Kokoxili earthquake to occur near the graben has a normal-faulting mechanism (Fig. 1). The inversion for three subevents (Fig. 7) favors separation of the moment release in time between the first two subevents, with very little moment release in subevent 2 within the first 5 sec. This also suggests a spatial separation between the subevents. We interpret these combined observations to indicate that the location of subevent 2 is within the graben and that coseismic rupture through the graben provided the means to transfer slip between the strike-slip segments. A schematic interpretation of the rupture process is shown in Figure 14.

The likely location of the oblique-faulting subevent within the step-over leads us to believe that the two strike-slip rupture segments mapped by Xu *et al.* (2002) are connected at depth by a through-going fault. Otherwise, the rupture would need to have jumped an ~10-km-wide step-over with no along-strike overlap between the strike-slip faults, unless the westernmost segment was ruptured by a large foreshock or aftershock. No foreshocks are indicated in global earthquake catalogs (Fig. 1), and there are no large aftershocks with strike-slip focal mechanisms located near the westernmost segment. A 10-km-wide step-over is larger than any previously observed to have been jumped by a seismic rupture (Wesnousky, 1988). The 1939 Erzincan, Turkey, earthquake appears to have jumped a 4-km-wide step-over, but it was stopped by a 10-km-wide step (Barka and Kadinsky-Cade, 1988). Harris and Day (1993) tested a case in two dimensions with the same rupture geometry as the strike-slip segments in the Kokoxili earthquake and with different step-over widths. Their results indicate that 5 km is the widest step-over that can be jumped (subsequently supported by Harris and Day [1999] using three-dimensional simulations). The stress field surrounding the crack tip is such that the triggering point for the second fault always occurs behind the edge of the first fault, so that the ruptures overlap along strike, for extensional step-overs. In the Kokoxili earthquake the second segment was triggered well ahead of the edge (Xu *et al.*, 2002; Figs. 1 and 14) rather than behind it, which again suggests linkage of the two segments. Harris and Day (1993) also found that step-overs larger than 1.5 km can only be jumped when the rupture is propagating at a supershear speed, while the data from Kokoxili suggest that supershear propagation did not occur until the rupture was fully transferred to the second segment (see the subsection on rupture dynamics and Fig. 14). However, the source time function of the earthquake (Fig. 7) indicates a pause in the moment release lasting for several seconds. While the inversion would not necessarily detect very low levels of slip, this could indicate a significant delay in the triggering of the second rupture segment. Harris and Day (1993) found that triggering delays of 3–5 sec, such as we observe here, occur for extensional step-overs 2–4 km wide (in the supershear case only). Therefore, the crossover fault in the Kokoxili step-over may not have completely linked the two rupture segments.

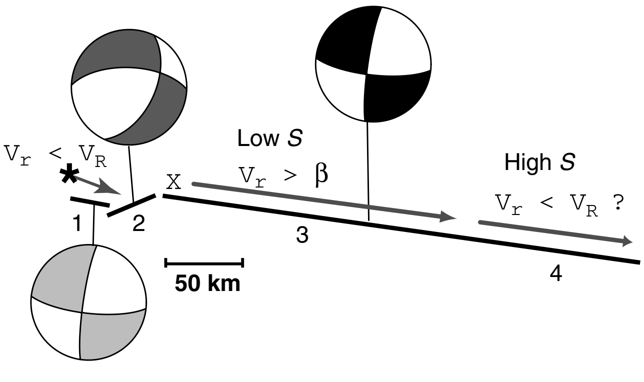

Figure 14. Schematic illustration of our interpretation of the Kokoxili rupture process. The arrows indicate direction of rupture propagation. The numbers refer to the fault segments of the four-segment rupture model (Fig. 15). The X indicates the inferred location of transition to super-shear rupture, which is shown at the beginning of fault segment 3. This location corresponds to $x = 48$ km in Figure 10, since fault segment 2 intersects segment 3 at this point. In our fault model we allowed some overlap between segments 1 and 3, but there is little slip on segment 3 until the intersection point of segment 2. V_R is the Rayleigh velocity, V_r is the rupture velocity, β is the shear-wave velocity, and S is the dimensionless strength parameter discussed in the text.

Rupture Velocity Variability and the Probability of Supershear Rupture

All our distributed-slip models used a fixed rupture velocity on each segment, with an average of 3.6 km/sec on the main segment providing the best overall data fit. Numerical results (e.g., Day, 1982; Andrews, 1985; Okubo, 1989) show that rupture speeds for mode II shear cracks can only be either lower than the Rayleigh velocity ($V_r < V_R$) or higher than the shear velocity but not exceeding the P-wave velocity ($\beta < V_r < \alpha$). The range of rupture velocities favored by the teleseismic data for the Kokoxili earthquake therefore implies supershear rupture.

A problem with all our distributed-slip models is that they appear to require a large patch of slip (up to 6 m) ~400 km to the east of the rupture initiation, which is past the eastern edge of the mapped surface rupture (Xu *et al.*, 2002). This asperity is also not required to match available geodetic data (Lasserre *et al.*, 2003). It is possible that substantial slip east of the mapped rupture may have been missed in the remote and difficult terrain, or perhaps this asperity represents slip at depth that did not reach the surface. However, it is more likely that this asperity is an artifact resulting from some inappropriate assumption of the simplified model that we have used. The increasing complexity and branching in the rupture toward its eastern termination, such as the rupture branching onto the Kunlun Pass fault (van der Woerd *et al.*, 2002a; Xu *et al.*, 2002) or the presence of significant reverse faulting there (P. Tapponnier and Y. Klinger, personal comm., 2003), might introduce spurious slip because we have fixed the focal mechanism on each model segment. Alternatively, the modeled slip might be real but its location incorrect, because of unmodeled variation in the rupture velocity.

In the finite-fault model the timing of large-slip asperities is well controlled by the waveforms, but the location of these asperities depends on the assumed rupture velocity. The best-fitting average rupture velocity determined by the inversion is controlled by the strongest asperity on the fault since this makes the largest contribution to the recorded waveforms. If significant variations in rupture velocity occur, then smaller asperities could be shifted in position on the fault. The source time function obtained from our point-source analysis contains a secondary peak that occurs at ~90 sec. A secondary peak of ~4 m also occurs in the surface-rupture observations (Fig. 11) at about $x = 320$ km. Both of these features could be associated with the asperity at $x = 400$ km in the finite-fault model. If so (and assuming that the surface-slip observations are well constrained), then the rupture must have slowed substantially after the rupture front passed the largest asperity at $x = 250$ km. We investigate this possibility by including a fourth fault segment in the finite-fault inversion with the same orientation and focal mechanism as segment 3, but allowing for a different rupture velocity. To fit the location of the high slip in the model within the observed surface rupture requires that the rupture velocity on fault segment 4 to be not much greater than 2.0 km sec^{-1}.

We show a four-segment model in Figure 15. This model still predicts more slip on this portion of the Kunlun fault than observed at the surface (Fig. 11). Some slip still persists past the end of the observed surface rupture, but it is of much smaller amplitude than is shown in Figure 12. In addition, slip appears to extend to somewhat greater depth in this region. The variance reduction for this model is quite similar to that for the model shown in Figure 12 (0.3% lower), and there is no visible difference in the data fits. Thus this model is an equally valid representation of slip in the earthquake, and one that fits the observed surface rupture better. Had we employed a more complicated inversion process, allowing slip to occur on fault nodes after passage of the rupture front, then a model similar to Figure 15 may have been identified as the optimal model. However, the teleseismic data cannot distinguish between a slowing rupture front and a constant rupture speed.

The rupture velocity on fault segment 4 (2.0 km sec^{-1}) is more typical of continental crustal earthquakes than the very high value inferred for segment 3. This slowing could be related to the branching of the rupture onto the Kunlun Pass fault, where it bends away from the Kunlun range front. The fault may therefore pass through upper crustal rocks having distinctly different elastic properties. The rupture velocity at fault branches can also be affected by stress interactions between the two rupture segments (e.g., Kame *et al.*, 2003).

Rupture Dynamics: Fracture Energy

Our models are purely kinematic, but we can use the results to investigate the dynamics of the rupture process of the Kokoxili earthquake. Studies of the earthquake energy budget are fundamental to the understanding of the dynamic rupture process. Large uncertainties in measurements of stress drop and radiated energy combine with the use of simplistic models to limit the constraints provided, and the scaling of radiated energy remains controversial (e.g., Abercrombie, 1995; Ide and Beroza, 2001). Abercrombie and Rice (in press) addressed this issue and demonstrated that present information does not constrain the scaling of the rupture process, and both scale-dependent and scale-independent models of earthquake nucleation are consistent with the observations. They calculated a parameter G' that is a good approximation to the fracture energy (per unit area) G under plausible stress conditions. $G' = G$ if the final dynamic stress equals the final static stress. Abercrombie and Rice (in press) found that G' increases from $\sim 10^3$ to 10^4 J m^{-2} for small earthquakes, consistent with laboratory measurements, to several MJ m^{-2} for large earthquakes with average slip $\bar{D} \geq 0.5$ m. The values for large earthquakes are in good agreement with those from dynamic inversions (e.g., Beroza and Spudich 1988; J. R. Rice *et al.*, unpublished manuscript, 2004).

Following Abercrombie and Rice (in press), we can calculate G' for the Kokoxili earthquake,

$$G' = \frac{\bar{D}}{2}\left(\Delta\sigma - \frac{2\mu E_s}{M_o}\right), \tag{4}$$

where $\Delta\sigma$ is the static stress drop, M_o is the scalar moment, μ is the shear modulus, $\bar{D}$ is the mean slip, and E_s is the radiated seismic energy. The static stress drop, $\Delta\sigma = 2M_o/\pi LW^2$ (Kanamori and Anderson, 1975), can be estimated from our fault model, where L is the total rupture length and W is the width. Using $M_o = 5.3 \times 10^{20}$ N m, $\mu = 30$ GPa, $L = 400$ km, and $W = 15$ km, we obtain $\Delta\sigma = 3.75$ MPa and $\bar{D} = 2.9$ m. The preliminary estimate of the radiated energy for the earthquake from teleseismic records (USGS NEIC) is 3.2×10^{16} J. Hence we obtain $G' \sim 0.2$ MJ m^{-2}. This is at the low end of the range obtained for large earth-

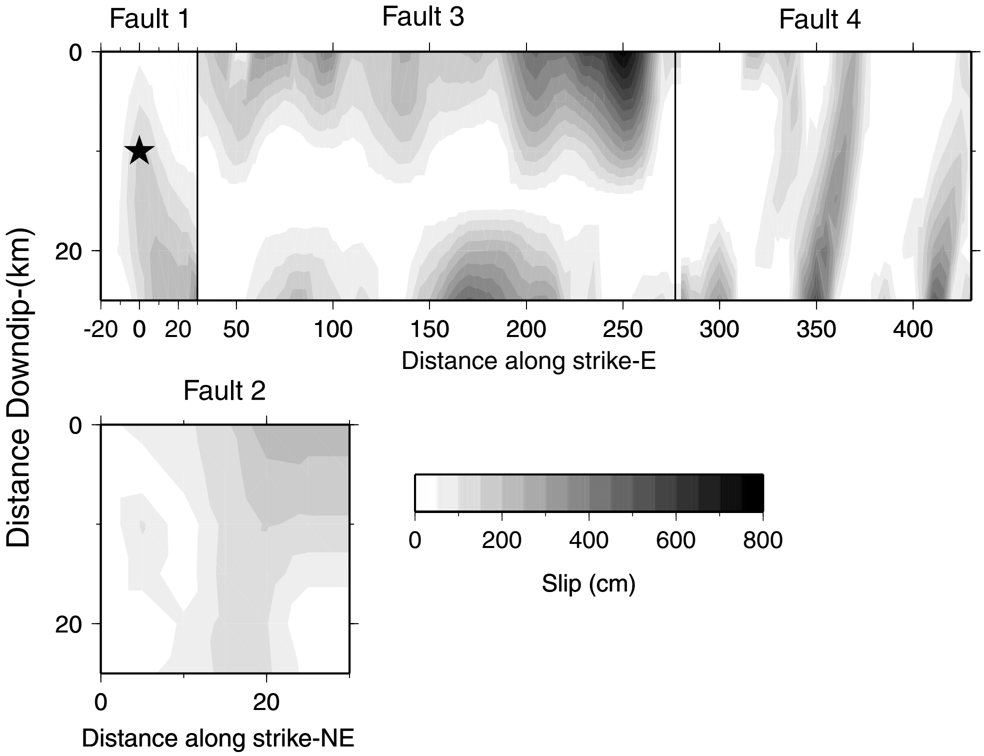

Figure 15. Slip distribution on a model with four fault segments. Fault segment 4 replaces the easternmost portion of segment 3 from the previous models. The coordinate system is the same as in Figures 10–12. Focal mechanism on segment 4 is constrained to be the same as segment 3, and the rupture velocity on this segment is 2.0 km $\sec^{-1}$. The model fits the *P* waves only slightly worse than the model shown in Figure 12 and fits the observed surface rupture better since the majority of the slip on segment 4 is moved farther west. Other details are similar to Figure 12.

quakes by Abercrombie and Rice (in press) and references therein. Teleseismic estimates of radiated energy are systematically lower than regional estimates (e.g., Pérez-Campos and Beroza, 2001; Boatwright *et al.*, 2002), but increasing E_s would decrease the size of G' still further. The high ratio of $E_s/M_o \sim 6 \times 10^{-5}$ and the low average fracture energy are consistent with the high rupture velocity. In numerical models of crack propagation, the crack accelerates as the shear resistance, that is, the energy needed to extend the fracture, decreases (e.g., Andrews, 1985; Okubo, 1989). Assuming that the rupture velocity of the Kokoxili earthquake reaches supershear velocity, we can use these models to make inferences about the initial stress state on the Kunlun fault.

In the numerical simulations of growing shear cracks, the crack half-length for transition from subshear to supershear rupture speeds, L_s, depends on the dimensionless strength parameter, S (Andrews, 1976, 1985). If we again assume that the final dynamic stress equals the final static stress, then

$$S = \frac{(\sigma_y - \sigma_0)}{\Delta\sigma}, \tag{5}$$

where σ_y is the fault yield stress and σ_0 is the initial static shear stress. The form of the dependence of L_s on S was investigated by Andrews (1976, 1985) and later by Okubo (1989) using a more complicated friction law. For $S \geq \sim 1.8$, crack propagation at greater than the Rayleigh speed cannot occur, and the transition to $V_r > \beta$ occurs sooner for smaller values of S. Andrews (1976, 1985) expressed L_s in terms of L_c, the critical crack half-length for extension, at which the available energy just balances the fracture energy required to lengthen the crack. In terms of the critical fracture energy (per unit area) G_c for crack extension at one end,

$$L_c = \frac{4}{\pi}\,(1 - \beta^2/\alpha^2)\,\frac{\mu G_c}{\Delta\sigma^2} \tag{6}$$

for mode II cracks. This equation differs by a factor 2 from that given in Andrews (1976) because he defined G_c as applying to only one side of the crack.

If we assume a simple crack model of rupture, then we can use equations (5) and (6) to obtain an estimate of G_c. Using the same estimates of L, W, μ, M_o, and $\Delta\sigma$ as before, and assuming $\alpha = \sqrt{3}\beta$, we have $G_c \sim 550 L_c$, where G_c is in joules per meter squared and L_c is given in meters. To obtain G_c we must first estimate L_c. In the numerical simulations the ratio L_c/L_s varies widely with S. For example, Andrews (1985) tested values of S ranging from 0.5 to 1.0 and found that the beginning of the transition to supershear rupture speed occurred at crack half-lengths $L_s \sim (3–20)\ L_c$. Okubo (1989) obtained similar results. Thus, even for these values of S, there is about an order of magnitude uncertainty in the location of the rupture velocity transition. For larger values of S approaching the theoretical limit of 1.8, L_s/L_c goes to infinity and the implied L_c would rapidly approach zero.

Assuming unilateral rupture propagation for the Kokoxili earthquake, we choose a value for L_s by examining the source time function of Figure 7 and comparing it with the slip distribution. The first two subevents of the earthquake span about 15 sec, and then moment release begins to increase very abruptly ~18 sec after initiation, at the beginning of subevent 3. In the slip distribution (Fig. 12), the rise in moment release rate corresponds with the first appearance of slip on fault segment 3 at about $x = 50$ km. Due to the complicated rupture geometry, there is some uncertainty as to the exact path of rupture propagation during the beginning stages, but a reasonable assumption is that the rupture front propagated ~50 km in the first 18 sec, consistent with an average rupture velocity of 2.8 km sec^{-1}. Thus we take the beginning of the slip in the third subevent as the rupture velocity transition, that is, $L_s = 50$ km. For the values of S in the range tested by Andrews (1985), $L_s = 50$ km corresponds to $L_c = 2.5–17$ km, giving us a range for G_c of 1.3–9.4 MJ m^{-2}, which is similar to other published values for large earthquakes (Niu, 1984; Abercrombie and Rice, in press). However, it is considerably higher than the estimate obtained earlier from the radiated energy. Since we have assumed that the final static and final dynamic stresses are the same, G_c should be equivalent to G'.

A discrepancy between the two fracture energy estimates might arise if the Kokoxili rupture was not entirely unilateral or because the rupture was not continuous from the hypocenter. For example, dynamic triggering may have caused the rupture front to jump ahead on fault segment 3, which would provide an alternative explanation for the high rupture velocity. Both of these factors would cause our inferred L_s (and hence L_c) to be an overestimate. However, if we accept the value of fracture energy obtained from the radiated energy, then S would need to be significantly larger. To obtain $G_c = 0.2$ MJ m^{-2} in equation (6) requires $L_c =$ 362 m, or $L_c/L_s \sim 7 \times 10^{-3}$. The form of the dependence of L_s on S therefore would suggest that S lies in the range 1.3–1.5 (see Andrews, 1985; Xia *et al.*, 2004). There is no *a priori* reason to assume that S must lie in the range tested in the numerical simulations, but there are reasons to assume that S should normally be closer to the limit for supershear rupture propagation. This could be the case, for example, if substantial reduction in the friction coefficient occurs at very small (micrometer-level) slips (Abercrombie and Rice, in press). Also, supershear rupture propagation has not been reported for most large earthquakes (as would be expected for $S \ll 1.8$). Therefore $S = 1.3–1.5$, as implied as implied by the large radiated energy, could still be well below the norm for crustal faults. Using these values for S in equation (5), we can then estimate a value for the strength excess $(\sigma_y - \sigma_0)$ on the Kunlun fault of 4.9–5.6 MPa.

From these considerations, it appears that the Kokoxili earthquake had a lower fracture energy than earthquakes of comparable size. For example, our estimate is 1–2 orders of magnitude lower than that obtained by Tse *et al.* (1985) or Rudnicki (1980) for the 1857 Fort Tejon, California, earthquake. The November 2002 Denali fault (Alaska) earthquake had a slightly lower value of $E_s/M_o = 4.5 \times 10^{-5}$ and a significantly higher value of $G' = 10–20$ MJ m^{-2} (Harvard CMT catalog M_o, E_s from the NEIC Web site, and source dimensions from Dreger *et al.* [2004]). These observations are consistent with the longer surface rupture and higher rupture velocity of the Kokoxili earthquake. Comparison with other recent large strike-slip earthquakes does not yield consistent patterns from the teleseismic parameters, suggesting that as yet the measurement uncertainties are too large and the number of well-studied earthquakes too small to generalize.

Rupture Dynamics: Along-Strike Variability

Our modeling enables us to resolve three distinct segments of the rupture on the main Kunlun fault (segments 3 and 4 in our model) with different dynamic behavior. In the west is a region of low slip, low stress drop, and high (supershear) rupture velocity. In the center is the region of high slip, high stress drop, and either average or high rupture velocity. In the east is a second region of low slip and low stress drop but with an average to low rupture velocity (segment 4). These observations imply a significant variation in friction and stress along the strike of the fault.

The distribution of aftershocks correlates with the slip distribution in the mainshock. The total number of aftershocks is very low. In the 18 months following the earthquake, the largest aftershock had M_w 5.6, and only 15 aftershocks with $m_b \geq 5.0$ have been recorded, although a few might have been missed due to the remote location. Velasco *et al.* (2000) studied the aftershock sequence of the 1997 Manyi earthquake and compared it to those from other large strike-slip ruptures. They found that earthquakes in Tibet typically have few aftershocks, and the Kokoxili earthquake is consistent with this trend. The distribution of the aftershocks of the Kokoxili earthquake is shown in Figure 1. They are remarkably clustered near and to the east of the area of largest slip in the earthquake (~93.3° E), and there are none in the area where supershear rupture velocity is suggested, assuming that the slower rupture speed for segment 4 is correct.

It is interesting to compare our observations from Kokoxili to those from more detailed studies of the 1999 İzmit, Turkey, earthquake. Supershear rupture was reported in the İzmit earthquake for 30–40 km to the east of the hypocenter, (e.g., Bouchon *et al.*, 2002; Sekiguchi and Iwata, 2002). Most slip inversions (Bouchon *et al.*, 2002; Delouis *et al.*, 2002; Li *et al.*, 2002) show relatively low levels of slip in this region, although it is beneath Sapanca Lake so the surface rupture is unclear (Barka *et al.*, 2002). The largest asperity on the fault in most of these studies occurs to the east of Sapanca Lake. There is a distinct gap in the aftershock distribution (Özalaybey *et al.*, 2002, their figure 6; Sekiguchi and Iwata, 2002) to the west of Sapanca Lake where the supershear speed is inferred. The aftershocks are strongly clustered in the immediate region of the hypocenter and to the east of Sapanca Lake. Hence, as for the Kokoxili earthquake, the inferred region of supershear rupture occurred where slip levels are relatively low and large aftershocks are absent. Preliminary investigations of the Denali fault earthquake also suggest a strong correlation between areas of relatively low slip, very high rupture velocity, and a lack of aftershock activity (Dreger *et al.*, 2004; Ozacar *et al.*, 2003).

These observations suggest changes in the frictional properties along active faults. The supershear rupture velocity in the western portion of the main Kokoxili rupture indicates a relatively low value for S (Scholz, 2002), and the relatively low slip implies a low stress drop. The parameter S can also be defined in terms of the strength drop $\Delta s = \sigma_y - \sigma_1$ as

$$S = \frac{\Delta s}{\Delta \sigma} - 1. \tag{7}$$

Hence the strength drop must also have been low there. A higher b-value (e.g., Wiemer and Wyss, 1997; Wyss *et al.*, 2000), and thus the observed absence of large aftershocks, may also be indicative of a low fault yield stress in this zone. This region may only slip unstably in smaller events unless dynamically forced by a large rupture propagating toward it. On the other hand, the slower rupture velocity in the eastern part of the Kokoxili rupture (east of the high-slip asperity) implies a higher Δs, with a similarly low stress drop (and hence significantly larger S; Fig. 14). The rupture velocity within the high-slip asperities does not seem well constrained in either the Kokoxili earthquake or for the İzmit and Denali fault earthquakes. If it is high, and perhaps also supershear, then a higher strength drop may not necessarily correlate with a high stress drop.

We can speculate as to the cause of this along-strike variability. Previous earthquakes on and around the Kunlun fault (for example, the Manyi earthquake) could result in variable initial stress. Changes in the orientation of the maximum regional compressive stress with respect to the fault strike will also affect the initial static stress. In addition, the frictional parameters could vary along strike. For example, the rheology could vary or the nature of the fault zone itself. Recent evidence has been accumulating that the Kunlun fault has accommodated much more left-lateral displacement than previously believed (Lasserre *et al.*, 1999; van der Woerd *et al.*, 2000), but the fault zone is probably not as well developed as the San Andreas system. Tapponnier *et al.* (2001) suggested that the Kunlun and other left-lateral faults in Tibet are propagating toward the east to accommodate internal deformation of the plateau, which would imply that the westernmost segment of the Kunlun fault is older than other segments. Laboratory and theoretical studies (e.g., Dieterich, 1981; Marone and Kilgore, 1993; Mair and Marone, 1999) have implied that G_c could be larger for faults having a thicker gouge zone because of an increase in the critical slip distance for fault weakening, d_c. For this to be the case, however, an increase of d_c by thick gouge material would need to counteract an expected opposite effect on the fault yield stress.

Conclusions

We use teleseismic body waves to obtain a rupture model for the November 2001 Kokoxili, Tibet (M_w 7.8), earthquake that is consistent with the geometry of the observed surface rupture. Our preferred model includes at least three subevents. The initiation of rupture, constrained by the first motions of P waves, is nearly pure strike slip. The second subevent has a large normal-faulting component, and then the main portion of the rupture (comprising ~95% of the moment release) is again strike slip. This model, in combination with the mapped surface offsets, suggests that the earthquake initiated along a 25-km-long fault segment in the far west. Slip was then transferred, by means of the oblique-normal subevent, through an ~45-km-long extensional graben, where little surface rupture was observed. Approximately 18 sec after the origin time, slip was initiated along the main trace of the Kunlun fault and propagated 350 km eastward along this segment for a duration of ~100 sec. Using a free finite-fault inversion without constraints from the surface observations, we are able to constrain the locations and strengths of the high-slip asperities. However, without use of the surface constraint we are unable to recover any moment release between these asperities.

We resolve a very high rupture velocity for a portion of the main fault segment (~3.6 km sec^{-1}). We also estimate a low value of fracture energy for the Kokoxili earthquake (0.2 MJ m^{-2}). Our inversion results, combined with the aftershock distribution, suggest a higher strength for the eastern portion of the main fault rupture compared to the western portion, which apparently failed during supershear propagation.

Acknowledgments

We benefited from discussions with P. Tapponnier, J. van der Woerd, Y. Klinger, C. Lasserre, and other members of the group at IPGP, Paris. C. Lasserre graciously provided details of their fault model based on InSAR data. We especially thank R. Dmowska, J. R. Rice, K. Felzer, and D. Bowman for interesting discussions. M. Vallée, M. Nettles, and an anonymous reviewer critically reviewed the manuscript. Most of the figures were produced by GMT and XMgr software.

References

Abercrombie, R. E. (1995). Earthquake source scaling relationships from -1 to 5 M_L using seismograms recorded at 2.5 km depth, *J. Geophys. Res.* **100,** 24,015–24,036.

Abercrombie, R. E., and J. R. Rice (in press). Can observations of earthquake scaling constrain slip weakening? *Geophys. J. Int.*

Abercrombie, R. E., M. Antolik, and G. Ekström (2003). The June 2000 M_w 7.9 earthquakes south of Sumatra: deformation in the India–Australia Plate, *J. Geophys. Res.* **108,** no. B1, 2018, doi 10.1029/2001JB000674.

Andrews, D. J. (1976). Rupture velocity of plane-strain shear cracks, *J. Geophys. Res.* **81,** 5679–5687.

Andrews, D. J. (1985). Dynamic plane-strain shear rupture with a slip-weakening friction law calculated by a boundary integral method, *Bull. Seism. Soc. Am.* **75,** 1–21.

Antolik, M., and D. S. Dreger (2003). Rupture process of the 26 January, 2001 M_w 7.6 Bhuj, India, earthquake from teleseismic broadband data, *Bull. Seism. Soc. Am.* **93,** 1235–1248.

Antolik, M., A. Kaverina, and D. S. Dreger (2000). Compound rupture of the great 1998 Antarctic Plate earthquake, *J. Geophys. Res.* **105,** 23,825–23,838.

Barka, A. A., and K. Kadinsky-Cade (1988). Strike-slip fault geometry in Turkey and its influence on earthquake activity, *Tectonics* **7,** 663–684.

Barka, A., H. S. Akyüz, E. Altunel, G. Sunal, Z. Çakir, A. Dikbas, B. Yerli, R. Armijo, B. Meyer, J. B. de Chabalier, T. Rockwell, J. R. Dolan, R. Hartleb, T. Dawson, S. Christofferson, A. Tucker, T. Fumal, R. Langridge, H. Stenner, W. Lettis, J. Bachhuber, and W. Page (2002). The surface rupture and slip distribution of the 17 August 1999 İzmit earthquake (*M* 7.4), North Anatolian fault, *Bull. Seism. Soc. Am.* **92,** 43–60.

Beroza, G. C., and P. Spudich (1988). Linearized inversion for fault rupture behaviour: application to the 1984 Morgan Hill, California, earthquake, *J. Geophys. Res.* **93,** 6275–6296.

Boatwright, J., G. Choy, and L. C. Seekins (2002). Regional estimates of radiated seismic energy, *Bull. Seism. Soc. Am.* **92,** 1241–1255.

Bouchon, M., and M. Vallée (2003). Observation of long supershear rupture during the $M_s = 8.1$ Kunlunshan (Tibet) earthquake, *Science* **301,** 824–826.

Bouchon, M., M. N. Toksöz, H. Karabulut, M.-P. Bouin, M. Dietrich, and M. Edie (2002). Space and time evolution of rupture and faulting during the 1999 İzmit (Turkey) earthquake, *Bull. Seism. Soc. Am.* **92,** 256–266.

Bowman, D., G. King, and P. Tapponnier (2003). Slip partitioning by elastoplastic propagation of oblique slip at depth, *Science* **300,** 1121–1123.

Centroid Moment Tensor (CMT) Catalog, www.seismology.harvard.edu/CMTsearch.html (last accessed August 2003).

Chen, W. P., C. Y. Chen, and J. Nábelek (1999). Present-day deformation of the Qaidam basin with implications for intra-continental tectonics, *Tectonophysics* **305,** 165–181.

Day, S. M. (1982). Three-dimensional simulation of spontaneous rupture: the effect of nonuniform pre-stress, *Bull. Seism. Soc. Am.* **72,** 1881–1902.

Delouis, B., D. Giardini, P. Lundgren, and J. Salichon (2002). Joint inversion of InSAR, GPS, teleseismic, and strong-motion data for the spatial and temporal distribution of earthquake slip: application to the 1999 İzmit mainshock, *Bull. Seism. Soc. Am.* **92,** 278–299.

Dieterich, J. (1981). Constitutive properties of faults with simulated gouge, in *Mechanical Behavior of Crustal Rocks*, American Geophysical Monograph **24,** 103–120.

Dreger, D., D. Oglesby, R. Harris, N. Ratchkovski, and R. Hansen (2004). Kinematic and dynamic rupture models of the November 3, 2002 M_w 7.9 Denali, Alaska, earthquake, *Geophys. Res. Lett.* **31,** L04605, doi 10.1029/2003GL018333.

Durek, J. J., and G. Ekström (1996). A radial model of anelasticity consistent with long-period surface wave attenuation, *Bull. Seism. Soc. Am.* **86,** 144–158.

Dziewonski, A. M., and D. L. Anderson (1981). Preliminary reference Earth model, *Phys. Earth Planet. Interiors* **25,** 297–356.

Eberhart-Phillips, D., P. J. Haeussler, J. T. Freymueller, A. D. Frankel, C. M. Rubin, P. Craw, N. A. Ratchkovski, G. Anderson, G. A. Carver, A. J. Crone, T. E. Dawson, H. Fletcher, R. Hansen, E. L. Harp, R. A. Harris, D. P. Hill, S. Hreinsdóttir, R. W. Jibson, L. M. Jones, R. Kayen, D. K. Keefer, C. F. Larsen, S. C. Moran, S. F. Personius, G. Plafker, B. Sherrod, K. Sieh, N. Sitar, and W. K. Wallace (2003). The 2002 Denali Fault earthquake, Alaska: a large magnitude, slip-partitioned event, *Science* **300,** 1113–1118.

Ekström, G. (1989). A very broadband inversion method for the recovery of earthquake source parameters, *Tectonophysics* **166,** 73–100.

Harris, R. A., and S. M. Day (1993). Dynamics of fault interaction: parallel strike-slip faults, *J. Geophys. Res.* **98,** 4461–4472.

Harris, R. A., and S. M. Day (1999). Dynamic 3D simulations of earthquakes on en-echelon faults, *Geophys. Res. Lett.* **26,** 2089–2092.

Henry, C., S. Das, and J. H. Woodhouse (2000). The great March 25, 1998, Antarctic Plate earthquake: moment tensor and rupture history, *J. Geophys. Res.* **105,** 16,097–16,118.

Hjörleifsdóttir, J., A. Kanamori, and J. Tromp (2003). Modeling recent large earthquakes using the 3-D global wavefield, Geophysical Research Abstracts CD-ROM 5, abstract 12707, European Geophysical Society, Nice, France.

Holt, W. E. (2000). Correlated crust and mantle strain fields in Tibet, *Geology* **28,** 67–70.

Ide, S., and G. C. Beroza (2001). Does apparent stress vary with earthquake size? *Geophys. Res. Lett.* **28,** 3349–3352.

Ji, C., D. Helmberger, and D. Wald (2002). Preliminary slip history of the 2002 Denali earthquake (abstract), *EOS* **83,** S72F–1344.

Kame, N., J. R. Rice, and R. Dmowska (2003). Effects of pre-stress state and rupture velocity on dynamic fault branching, *J. Geophys. Res.* **108,** no. B1, 2265, doi 10.1029/2002JB002189.

Kanamori, H., and D. Anderson (1975). Theoretical basis for some empirical relations in seismology, *Bull. Seism. Soc. Am.* **65,** 1073–1095.

Kaverina, A., D. Dreger, and E. Price (2002). The combined inversion of seismic and geodetic data for the source process of the 16 October 1999 M_w 7.1 Hector Mine, California, earthquake, *Bull. Seism. Soc. Am.* **92,** 1266–1280.

Kennett, B. L. N., and E. R. Engdahl (1991). Traveltimes for global earthquake location and phase identification, *Geophys. J. Int.* **105,** 429–465.

Kikuchi, M., and H. Kanamori (1982). Inversion of complex body waves, *Bull. Seism. Soc. Am.* **72,** 491–506.

King, G., D. Bowman, Y. Klinger, J. van der Woerd, P. Tapponnier, X. Xu, W. Chen, and W. Ma (2003). Slip-partitioned surface breaks for the 14 November 2001, M_w 7.8 Kokoxili earthquake, Geophysical Research Abstracts CD-ROM 5, abstract 04226, European Geophysical Society, Nice, France.

Lasserre, C., P.-H. Morel, Y. Gaudemer, P. Tapponnier, F. J. Ryerson, G. C. P. King, F. Métivier, M. Kasser, M. Kashgarian, L. Baichi, L. Taiya, and Y. Daoyang (1999). Postglacial left slip rate and past occurrence of $M \geq 8$ earthquakes on the western Haiyuan fault, Gansu, China, *J. Geophys. Res.* **104,** 17,633–17,651.

Lasserre, C., G. Peltzer, J. van der Woerd, Y. Klinger, and P. Tapponnier (2003). Coseismic deformation from the $M_w = 7.8$ Kokoxili earthquake from ERS InSAR data, Geophysical Research Abstracts CD-ROM 5, abstract 09104, European Geophysical Society, Nice, France.

Lay, T., and T. C. Wallace (1995). *Modern Global Seismology*, Academic, New York.

Li, S., and W. D. Mooney (1998). Crustal structure of China from deep seismic sounding profiles, *Tectonophysics* **288,** 105–113.

Li, X., V. F. Cormier, and M. N. Toksöz (2002). Complex source process of the 17 August 1999 İzmit, Turkey, earthquake, *Bull. Seism. Soc. Am.* **92,** 267–277.

Lin, A., B. Fu, J. Guo, Q. Zeng, G. Dang, W. He, and Y. Zhao (2002). Coseismic strike-slip and rupture length produced by the 2001 M_s 8.1 central Kunlun earthquake, *Science* **296,** 2015–2017.

Mair, K., and C. Marone (1999). Friction of simulated fault gouge for a wide range of velocities and normal stresses, *J. Geophys. Res.* **104,** 28,899–28,914.

Marone, C., and B. Kilgore (1993). Scaling of the critical slip distance for seismic faulting with shear strain and fault zones, *Nature* **362,** 618–621.

McNamera, D. E., D. J. Wald, and H. Benz (2002). Strong ground motion in central Alaska resulting from the Denali Fault *M* 7.9 earthquake of November 3, 2002 (abstract), *EOS* **83,** S72F–1350.

Meyer, B., P. Tapponnier, L. Bourjot, F. Métivier, Y. Gaudemer, G. Peltzer, G. Shunmin, and C. Zhitai (1998). Crustal thickening in Gansu-Qinghai, lithospheric mantle subduction, and oblique, strike-slip controlled growth of the Tibet plateau, *Geophys. J. Int.* **135,** 1–47.

Niu, H. (1984). Estimates of fracture parameters of earthquakes, *Pure Appl. Geophys.* **122,** 645–661.

Okubo, P. G. (1989). Dynamic rupture modeling with laboratory-derived constitutive relations, *J. Geophys. Res.* **94,** 12,321–12,335.

Ozacar, A. A., S. L. Beck, and D. H. Christensen (2003). Source process of the 3 November, 2002 Denali Fault (central Alaska) earthquake from teleseismic observations, *Geophys. Res. Lett.* **30,** no. 12, 1638, doi 10.1029/2003GL017272.

Özalaybey, S., M. Ergin, M. Aktar, C. Tapirdamaz, F. Biçmen, and A. Yörük (2002). The 1999 İzmit earthquake sequence in Turkey: seismological and tectonic aspects, *Bull. Seism. Soc. Am.* **92,** 376–386.

Peltzer, G., and F. Saucier (1996). Present-day kinematics of Asia derived from geologic fault rates, *J. Geophys. Res.* **101,** 27,943–27,956.

Peltzer, G., F. Crampe, and G. King (1999). Evidence of nonlinear elasticity of the crust from the $M_w = 7.6$ Manyi (Tibet) earthquake, *Science* **286,** 272–276.

Pérez-Campos, X., and G. C. Beroza (2001). An apparent mechanism dependence of radiated seismic energy, *J. Geophys. Res.* **106,** 11,127–11,136.

Rudnicki, J. W. (1980). Fracture mechanics applied to the Earth's crust, *Ann. Rev. Earth Planet. Sci.* **8,** 489–525.

Saikia, C. K. (1994). Modified frequency–wavenumber algorithm for regional seismograms using Filon's quadrature: modelling of *Lg* waves in eastern North America, *Geophys. J. Int.* **118,** 142–158.

Scholz, C. H. (2002). *The Mechanics of Earthquakes and Faulting*, Second Ed. Cambridge U Press, New York.

Sekiguchi, H., and T. Iwata (2002). Rupture process of the 1999 Kocaeli, Turkey, earthquake estimated from strong-motion waveforms, *Bull. Seism. Soc. Am.* **92,** 300–311.

Tapponnier, P., B. Meyer, J. P. Avouac, G. Peltzer, Y. Gaudemer, S. Guo, H. Xiang, K. Yin, and Z. Chen (1990). Active thrusting and folding in the Qilian Shan, and decoupling between upper crust and mantle in northeastern Tibet, *Earth Planet. Sci. Lett.* **97,** 382–403.

Tapponnier, P., X. Zhiqin, F. Roger, B. Meyer, N. Arnaud, G. Wittinger, and Y. Jingsui (2001). Oblique stepwise rise and growth of the Tibet plateau, *Science* **294,** 1671–1677.

Tse, S. T., R. Dmowska, and J. R. Rice (1985). Stressing of locked patches along a creeping fault, *Bull. Seism. Soc. Am.* **75,** 709–736.

van der Woerd, J., F. J. Ryerson, P. Tapponnier, Y. Gaudemer, R. Finkel, A.-S. Meriaux, M. W. Caffee, Z. Guoguang, and H. Qunlu (1998). Holocene left-slip rate determined by cosmogenic surface dating on the Xidatan segment of the Kunlun fault, *Geology* **26,** 695–698.

van der Woerd, J. F. J. Ryerson, P. Tapponnier, Y. Gaudemer, A.-S. Meriaux, R. C. Finkel, M. W. Caffee, Z. Guoguang, and X. Zhiqin (2000). Uniform slip rate along the Kunlun fault: implications for seismic behavior and large-scale tectonics, *Geophys. Res. Lett.* **27,** 2353–2356.

van der Woerd, J., A.-S. Mériaux, Y. Klinger, F. J. Ryerson, Y. Gaudemer, and P. Tapponnier (2002a). The 14 November 2001, $M_w = 7.8$ Kokoxili earthquake in northern Tibet (Qinghai Province, China), *Seism. Res. Lett.* **73,** 125–135.

van der Woerd, J., P. Tapponnier, F. J. Ryerson, A.-S. Meriaux, B. Meyer, Y. Gaudemer, R. C. Finkel, M. W. Caffee, Z. Guoguang, and X. Zhiqin (2002b). Uniform postglacial slip-rate along the central 600 km of the Kunlun Fault (Tibet), from ^{26}Al, ^{10}Be, and ^{14}C dating of riser offsets, and climatic origin of the regional morphology, *Geophys. J. Int.* **148,** 356–388.

van der Woerd, J., Y. Klinger, P. Tapponnier, X. Xu, W. Chen, W. Ma, and G. King (2003). Coeismic offsets and style of surface ruptures of the 2001 $M_w = 7.8$ Kokoxili earthquake (northern Tibet), Geophysical Research Abstracts CD-ROM 5, abstract 11,151, European Geophysical Society.

Velasco, A. A., C. J. Ammon, and S. L. Beck (2000). Broadband source modeling of the November 8, 1997, Tibet ($M_w = 7.5$) earthquake and its tectonic implications, *J. Geophys. Res.* **105,** 28,065–28,080.

Wald, D. J., and T. H. Heaton (1994). Spatial and temporal distribution of slip for the 1992 Landers, California, earthquake, *Bull. Seism. Soc. Am.* **84,** 668–691.

Wald, D. J., T. H. Heaton, and K. W. Hudnut (1996). Slip history of the 1994 Northridge, California, earthquake determined from strong-motion, teleseismic, GPS, and leveling data, *Bull. Seism. Soc. Am.* **86,** S49–S70.

Wesnousky, S. G. (1988). Seismological and structural evolution of strike-slip faults, *Nature* **335,** 340–343.

Wiemer, S., and M. Wyss (1997). Mapping the frequency–magnitude distribution in asperities: an improved technique to calculate recurrence times? *J. Geophys. Res.* **102,** 15,115–15,128.

Wittlinger, G., P. Tapponnier, G. Poupinet, J. Mei, S. Danian, G. Herquel, and F. Masson (1998). Tomographic evidence for localized lithospheric shear along the Altyn Tagh Fault, *Science* **282,** 74–76.

Wyss, M., D. Schorlemmer, and S. Wiemer (2000). Mapping asperities by minima of local recurrence time: San Jacinto–Elsinore faults, *J. Geophys. Res.* **105,** 7829–7844.

Xia, K., A. J. Rosakis, and H. Kanamori (2004). Laboratory earthquakes: the sub-Rayleigh-to-supershear rupture transition, *Science* **303,** 1859–1861.

Xu, X., W. Chen, W. Ma, G. Yu, and G. Chen (2002). Surface rupture of the Kunlunshan earthquake (M_s 8.1), northern Tibetan plateau, China, *Seism. Res. Lett.* **73,** 884–892.

Department of Earth and Planetary Sciences
Harvard University
Cambridge, Massachusetts 02138
(M.A., G.E.)

Department of Earth Sciences
Boston University
Boston, Massachusetts 02115
(R.E.A.)

Manuscript received 29 August 2003.